PCCP

ROYAL SOCIETY OF CHEMISTRY

PAPER

Cite this: *Phys. Chem. Chem. Phys.*, 2023, **25**, 2566

How do salt and lipids affect conformational dynamics of Aβ42 monomers in water?†

Brian Andrews, Thomas Ruggiero and Brigita Urbanc *

It is well established that amyloid β-protein (Aβ) self-assembly is involved in triggering of Alzheimer's disease. On the other hand, evidence of physiological function of Aβ interacting with lipids has only begun to emerge. Details of Aβ–lipid interactions, which may underlie physiological and pathological activities of Aβ, are not well understood. Here, the effects of salt and 1,2-dimyristoyl-*sn-glycero*-3-phosphocholine (DMPC) lipids on conformational dynamics of Aβ42 monomer in water are examined by all-atom molecular dynamics (MD). We acquired six sets of 250 ns long MD trajectories for each of the three lipid concentrations (0, 27, and 109 mM) in the absence and presence of 150 mM salt. Ten replica trajectories per set are used to enhance sampling of Aβ42 conformational space. We show that salt facilitates long-range tertiary contacts in Aβ42, resulting in more compact Aβ42 conformations. By contrast, addition of lipids results in lipid-concentration dependent Aβ42 unfolding concomitant with enhanced stability of the turn in the A21–A30 region. At the high lipid concentration, salt enables the N-terminal region of Aβ42 to form long-range tertiary contacts and interact with lipids, which results in formation of a parallel β-strand. Aβ42 forms stable lipid–protein complexes whereby the protein is adhered to the lipid cluster rather than embedded into it. We propose that the inability of Aβ42 monomer to get embedded into the lipid cluster may be important for facilitating repair of leaks in the blood-brain barrier without penetrating and damaging cellular membranes.

Received 28th October 2022,
Accepted 22nd December 2022

DOI: 10.1039/d2cp05044g

rsc.li/pccp

1 Introduction

Amyloid β-protein (Aβ) is best known for its role in Alzheimer's disease (AD), whereby soluble low-molecular-weight oligomers that lack ordered structure are posited to mediate Aβ-induced AD pathology.[1–3] Aβ is an intrinsically disordered protein (IDP) that lacks a native fold, a property in common with several other amyloidogenic proteins whose aberrant self-assembly into oligomers is associated with human diseases.[4] It is unclear how Aβ oligomers, in particular, trigger the complex AD pathology but the process likely involves their interaction with cellular membrane components and/or membrane damage,[5,6] which eventually leads to tau phosphorylation and formation of neurofibrillary tangles.[7] Of the two predominant alloforms, Aβ40 and Aβ42, the latter is associated with faster aggregation into amyloid fibrils[8,9] and produces oligomers that exert more toxic effects both *in vitro*[10,11] and *in vivo*.[12,13]

Many efforts toward finding the structural basis of Aβ toxicity and design anti-Aβ drugs have overshadowed accumulating evidence that full-length Aβ is not just an inert byproduct of sequential cleavages of amyloid precursor protein by β- and γ-secretases, but rather plays an essential physiological role by performing a series of physiological functions, including protecting the brain from viral and microbial infections, regulating activity at hippocampal synapses, and repairing leaks in the blood-brain barrier.[14] Antibacterial activity of human Aβ in cell cultures was reported by Soscia *et al.*[15] and later by Kumar and collaborators, who used mice and nematodes to demonstrate that bacterial cells were entrapped by human Aβ fibrils as a part of the antimicrobial defense.[16] White *et al.* showed that Aβ effectively prevented infection of cultured cells by two

Department of Physics, Drexel University, Philadelphia, Pennsylvania, USA. E-mail: bu25@drexel.edu

† Electronic supplementary information (ESI) available: Table S1: descriptions (number and concentrations of molecules) of simulated systems. Table S2: experimental and MD-derived $^3J(H^N, H^{C\alpha})$ coupling constants using four sets of Karplus parameters. Table S3: RMSE values between MD-derived and experimental $^3J(H^N, H^{C\alpha})$ constants and between sets of MD-derived $^3J(H^N, H^{C\alpha})$ constants. Fig. S1: RMSD of an Aβ42 monomer as a function of simulation time in all conditions. Fig. S2: distance between the N- and C-termini as a function of simulation time. Fig. S3: Karplus curves using the four sets of Karplus parameters. Fig. S4: comparison of MD-derived $^3J(H^N, H^{C\alpha})$ constants on an amino acid basis using 50 ns and 250 ns of simulation time. Fig. S5: comparison of experimental and MD-derived $^3J(H^N, H^{C\alpha})$ constants on an amino acid basis using all four sets of Karplus parameter sets. Fig. S6: omparison of experimental (277 K) and MD-derived (277 and 300 K) $^3J(H^N, H^{C\alpha})$ constants on an amino acid basis. Fig. S7: helix, bridge, coil, strand, and turn secondary structure propensities for each amino acid residue. Fig. S8: visualization of a DMPC molecule with emphasis on atoms used in analyses. Fig. S9: differences between average minimum distance between Aβ42 amino acid residues and different atom groups of the closest DMPC molecule in different solvent. See DOI: **https://doi.org/10.1039/d2cp05044g**

strains of the influenza virus.[17] This antiviral action involved Aβ binding viral particles into aggregates, whereby Aβ42 was more effective than Aβ40.[17,18] A similar study by Bourgade and collaborators showed that Aβ42 prevented herpes simplex virus 1 infections.[19] Sealing leaks in the blood-brain barrier has been shown to involve Aβ anchoring itself onto cellular membranes and thereby increasing adherence between the red blood cells and endothelial cells.[14] Thus, both in the context of AD and normal physiological activity, Aβ42 mediates its function by interacting with cellular membrane components.

Whereas substantial evidence shows that Aβ42 interacting with lipid components underlies the activity of this peptide in health and disease, the mechanisms and pathways of Aβ42 interactions with cellular membranes remain unresolved. In the context of Aβ42-induced membrane damage, the pathway of insertion of Aβ (and other human disease-related IDPs) from the aqueous phase into the hydrocarbon core of the lipid bilayer is not well understood. The role of free lipids in this process has recently been elucidated by La Rosa and collaborators, who developed a diffusion-reaction model of a lipid-assisted proteins transport from water into the lipid bilayer and tested this model on amylin by measuring leakage of a fluorescent probe across the lipid bilayer of large unilamellar vescicles and conducting MD simulations.[20] A follow-up study, Sciacca *et al.* provided more evidence by experimentally examining an insertion of amylin, Aβ40, and α-synuclein into lipid bilayers and proposed the lipid-chaperone hypothesis, whereby the protein first forms a complex with free lipids, followed by an insertion of this complex into the membrane.[21] Using molecular dynamics (MD) simulations, Fatafta and collaborators explored this hypothesis by studying Aβ42 monomer interacting with one and three POPC lipids, followed up by identifying a stable Aβ42–lipid complex and monitoring its interactions with the lipid bilayer.[22] Aβ42 was shown to form stable complexes with one as well as three POPC lipids, but was reported to undergo disorder-to-order transition into α-helical or β-sheet structure only when interacting with three lipids.[22] The Aβ42–POPC complex adsorbed onto the surface of lipid bilayer, increasing the β-sheet content in Aβ42, however, no spontaneous insertion of the complex into the bilayer was observed on a time scale of one microsecond.[22] These results are consistent with an experimental observation that Aβ oligomers bind more avidly to the membranes than Aβ monomers,[23] which are generally not considered neurotoxic and may be thus associated with a physiological function.

An early MD study by Caves and collaborators of a natively folded protein, crambin, demonstrated that conformational sampling is improved when multiple trajectories with different initial conditions are used instead of a single long trajectory.[24] A more recent study by Knapp *et al.* noted that conclusions drawn from a single long MD trajectory are often not reproducible and proposed that, as a good rule of thumb, 5–10 trajectories are used to avoid erroneous conclusions.[25] As an IDP, Aβ42 populates a large ensemble of conformations that are sensitive to the nature of the solvent, ionic concentration, pH, osmolytes and crowders, resulting in rugged free energy landscapes.[26] This large number of degrees of freedom translates into a large phase space, which represents an additional sampling challenge when characterizing the conformational dynamics of Aβ42 by MD.[27] The strategy of using a large number of replicas in MD simulations to improve the phase space sampling was used by some of us in earlier studies of Aβ40 and Aβ42 monomers, dimers, trimers, tetrames, and pentamers using OPLS-AA/L with TIP3P water.[28,29] In this paper, we employ CHARMM36m[30] which was shown to be one of the most reliable MD force fields for modeling short unfolded peptides,[31–34] although lacking amino acid specificity in reproducing experimentally-derived Ramachandran distributions of residues in water.[35] *In vivo*, Aβ42 exerts its activity in the presence of physiological levels of salt and other biomolecules. We here ask, to which extent physiological levels of salt and the presence of free lipids affect Aβ42 folding dynamics. To model lipids, we select DMPC molecules, *i.e.* zwitterionic lipid molecules of the phosphocholine (PC) type, which dominate the neuronal soma and brain endothelial brain cell membranes.[36,37] We acquire six sets of MD trajectories of Aβ42 monomer interacting with 0, 12 and 48 DMPC lipids, each in the absence and presence of 150 mM NaCl, each set comprising ten 250 ns-long MD replica trajectories to feed structural analysis. Our findings show that salt exerts a significant effect on Aβ42 folding, giving rise to more compact conformations, whereas the presence of lipids favors more extended conformations. Addition of both, salt and lipids, enhances the ruggedness of the free energy landscapes of Aβ42 monomer conformations. Importantly, our results indicate that Aβ42 forms stable complexes with 12 as well as 48 lipids, whereby Aβ42 remains adhered to the surface of the lipid cluster without penetrating it.

2 Methods

2.1 Molecular dynamics simulations

Fully atomistic MD simulations in explicit solvent were performed with GROMACS 2021.1[38–44] using CHARMM36m force field with its specific TIP3P water model[30,45–47] for proteins, water, and ions and the CHARMM36 lipid force field for DMPC lipid molecules.[48] Six sets of MD trajectories were acquired: Aβ42 monomer in (i) pure water, (ii) water with 12 DMPC lipid molecules (27 mM or 18.3 g L^{-1}), (iii) water with 48 DMPC lipid molecules (109 mM or 73.8 g L^{-1}); sets (iv)–(vi) corresponded to (i)–(iii) each with an addition of 150 mM NaCl to model the physiological salt concentration. The number and concentrations of molecules in each set of simulations are outlined in Table S1 (ESI†). Ten MD trajectories of set (i) were acquired first from ten distinct Aβ42 monomer conformations derived from trajectories generated by discrete molecular dynamics (DMD) simulations with DMD4B-HYDRA force field,[49,50] followed by a conversion to an all-heavy-atom conformations using our in-house software *protsView*. Each resulting conformer was then placed in a $(9\ \text{nm})^3$ simulation box corresponding to a concentration of 2.27 mM. The N- and C-termini of each Aβ42

molecule corresponded to NH_3^+ and COO^-, respectively. Three Na^+ ions were added to Aβ42 molecule to neutralize each system. The addition of hydrogen atoms to Aβ42 conformation, the addition of ions to the solvent, and the resolution of atom collisions was performed within GROMACS during the preparation and energy minimization steps. The Verlet cutoff scheme[51] and a time step of 2 fs were used during the equilibration and production steps. Energy minimization was performed with the steepest descent method for 100 000 steps and was followed by a 200 ps-long equilibration step at 300 K and 1.0 bar. All production runs used the velocity rescale thermostat[52] with a coupling strength 0.1 ps and a Berendsen barostat[53] with a coupling strength 1.0 ps. This combination of thermostat and barostat is representative of a weak coupling algorithm that might introduce artifacts into constant pressure simulations.[54] Nontheless, the combination of the velocity rescale thermostat and Berendsen barostat with the coupling strengths used in our simulations was recently shown to perform *on par* with the most reliable thermostat/barostat options except for volume fluctuations and compressibility (which are not of interest in this study).[55] The final conformations of the trajectory set (i) after 250 ns-long production runs were then used to generate sets (ii)–(vi) by insertion of ions and/or lipid molecules. The inserted molecules replaced the solvent molecules with which overlaps occurred. An additional solvation step was conducted to ensure the correct final solvent density, followed by 250 ns production runs for all six sets of trajectories. For each of six sets of MD simulations, we thus generated ten distinct 250 ns-long MD trajectories, resulting in 17.5 μs of MD simulations in total.

Additional ten 250 ns-long trajectories of an Aβ42 monomer in water with 150 mM salt were acquired at 277 K were to facilitate comparison to experimental data. All other parameters used in these simulations were the same as in simulations at 300 K.

2.2 Structural analysis

2.2.1 Comparison to experimental observables. $^3J(H^N, H^{C_\alpha})$ coupling constants are calculated using the Karplus relation[56] and four sets of Karplus parameters: Hu and Bax,[57] Vuister and Bax,[58] Habeck *et al.*,[59] and Vögeli *et al.*[60] Ramachandran distributions for each amino acid in each trajectory are generated from simulations of an Aβ42 monomer in pure water and in 150 mM salt using 50–250 ns of simulation time. The coupling constant for each amino acid is then calculated as an ensemble average of the Karplus relation and the Ramachandran distribution as in the following:

$$^3J(H^N, H^{C_\alpha}) = \sum_\phi J(\phi) \sum_\psi P(\phi, \psi) \quad (1)$$

where $J(\phi)$ is the Karplus relation and ϕ and ψ are the dihedral angles. $^3J(H^N, H^{C_\alpha})$ constants calculated from each trajectory (for pure water and salt conditions separately) is then averaged and error bars are calculated as the Standard Error of the Mean using averages from each trajectory.

2.2.2 Free energy landscapes. Free energy landscapes were calculated using the two-dimensional distribution of five pairs of reaction coordinates: solvent accessible surface area (SASA) of hydrophobic residues (I, V, F, L, M, C, and A) and distance between N- and C-terminal C_α atoms (N–C Distance or N2CD), N2CD and radius of gyration (R_g), hydrophobic SASA and R_g, hydrophobic SASA and contact order,[61] and R_g and contact order. SASA was calculated using a radius of 1.4 Å and does not include protein–lipid interactions. The value of each reaction coordinate was calculated every 2 ps during times 200–250 ns. Normalized two dimensional distributions, $P(X_1,X_2)$, are then generated from these calculations where X_1 and X_2 represent the listed reaction coordinates. The free energy is then calculated as $\beta W(X_1,X_2) = -\ln P(X_1,X_2) + M$, where M is a constant.

2.2.3 Secondary structure analysis. Secondary structure of Aβ42 were determined using the STRIDE algorithm[62] implemented in VMD.[63] Our analysis considers 5 types of secondary structure: β-strand, turn, coil, bridge, and α-helix. Secondary structure propensities were calculated as averages over times 200–250 ns of all ten replicas, sampling every 2 ps, and normalized by the number of structures considered. Error bars were then calculated as Standard Error of the Mean (SEM) using the averages from 200–250 ns of each trajectory.

2.2.4 Contact maps. Although lacking a stable tertiary structure, intrapeptide contact maps of the Aβ42 monomer are calculated in VMD to discern how the environment affects that way Aβ42 interacts with itself. Amino acids are determined to be in contact with one another when the respective pairs of C_α atoms are within 6 Å. The contact maps show contact probabilities and SEM above and below the main diagonal, respectively. To better highlight the effects of the environment on contacts in different conditions, contact map differences are then calculated by subtracting two sets of contact probabilities. In contact map differences, red indicates stronger contacts in conditions relative to the control and blue indicates stronger contacts in the control (*i.e.* pure water). Probabilities and SEM values were calculated every 2 ps during times 200–250 ns of each trajectory.

2.2.5 Minimum protein–lipid distance. For Aβ42 monomer simulations with lipids, the minimum distance between any atom of each amino acid residue in Aβ42 and the DMPC head group heavy N atom, the phosphor group P atom, and tail group carbon atoms were calculated using the mdtraj python package.[64] Sampling was performed at 2 ps intervals during times 50–250 ns. The average minimum distances for relative to each lipid group were then averaged and error bars were generated by calculating SEM using the averages from each of the ten individual trajectories in each lipid and salt concentration.

2.2.6 Interface area of protein–lipid complex. The surface area over which the protein and lipid clusters interact was calculated by caculating (1) the total SASA of the protein (lipids are treated as solvent), (2) the total SASA of the lipid cluster (protein is counted as solvent), and (3) the total SASA of the protein–lipid complex. The interface area of the two groups can

then be calculated by taking the sum of (1) and (2), subtracting by (3), and dividing the result by two to account for counting the interaction area twice. SASA was calculated as implemented in VMD with a cutoff of 1.4 Å. Note that in case (1), the lipids, salt, and water are all considered to be the solvent. Analogously, note that in case (2), the water, salt, and the Aβ42 monomer are all considered to be the solvent. Sampling was performed at 2 ps intervals during times 50–250 ns and were used to construct normalized distributions of (1)–(3) and the interface area.

2.2.7 Lipid cluster size distribution. A DMPC molecule is considered to be within a cluster if the distance between any atoms belonging to different DMPC molecules are within 3.5 Å. Histograms of cluster sizes are then generated from simulations with nonzero lipid concentration, with and without physiological salt, sampling every 2 ps during times 50–250 ns. The final size distribution is then the average of the ten distributions from each set of lipid and salt conditions. Error bars are calculated as the SEM using the values of the distributions from each individual trajectory for in each lipid and salt concentration.

3 Results

We here examine by means of explicit-solvent MD the effect of the physiological salt concentration on conformational dynamics of fully-atomistic Aβ42 monomers and address the modalities of Aβ42 monomer interactions with lipids in the absence of and presence of salt. Aβ42–lipid interactions are expected to play an important role in Aβ42-mediated disruption of cellular membranes in the context of AD. Interactions between Aβ42 and lipids play an important role in posited physiological functions of Aβ42, which including the repair of leaks in the blood–brain barrier as well as antiviral and antimicrobial activities.[14]

In the previous work, Barz and Urbanc structurally analyzed large numbers of Aβ40 and Aβ42 monomer and dimer MD trajectories using OPLS-AA/L[65,66] with TIP3P and SPCE water models.[28] This study was extended by Voelker, Barz, and Urbanc, who examined fully atomistic conformations of Aβ40 and Aβ42 monomers through pentamers using OPLS-AA/L in explicit TIP3P water model. We here examine the effect of salt and DMPC lipids on fully atomistic Aβ42 monomer conformations using CHARMM36m and its innate TIP3P water model, which was shown to perform optimally based on comparison to available spectroscopic data on short unfolded peptides when compared to other modern force fields.[31,33–35,67]

We acquired six sets of MD trajectories, following the protocol described in Methods. Sets (i)–(iii) correspond Aβ42 monomer in pure water, water with 12 DMPC lipid molecules (27 mM), and water with 48 DMPC lipid molecules (109 mM), respectively. Sets (iv)–(vi) are analogous to sets (i)–(iii), respectively, with added 150 mM NaCl to model the physiological salt concentration. DMPC is a zwitterionic phospholipid molecule, abundant in mammalian membranes, and was used as the main component of biomimetic lipid vesicles in experiments by Williams and collaborators to demonstrate how Aβ42 oligomers affects the membrane permeability.[68,69] Fig. 1(A) shows the simulation setup we use in our simulations of Aβ42 (red) with initially randomly placed DMPC lipids (gray) and salt ions (blue and cyan). The subsequent time evolution of this system is displayed in Fig. 1(B) and (C).

The sequence of Aβ42 is $DAEFRHDSGY_{10}$ $EVHHQKLVFF_{20}$ $AEDVGSNKGA_{30}$ $IIGLMVGGVV_{40}$ IA_{42}.

At physiological pH, Aβ42 with 6 negatively charged and 3 positively charged amino acid residues is overall negatively charged, $-3e$. The structural analysis of the six trajectory sets is provided below. In the description of our results, we use the following abbreviations: NTR for the N-terminal region (D1–D7), CHC for the central hydrophobic cluster (L17–A21), CFR for the central folding region (A21–A30), MHR for the mid-hydrophobic region (I31–V36), and CTR for the C-terminal region (V39–A42).

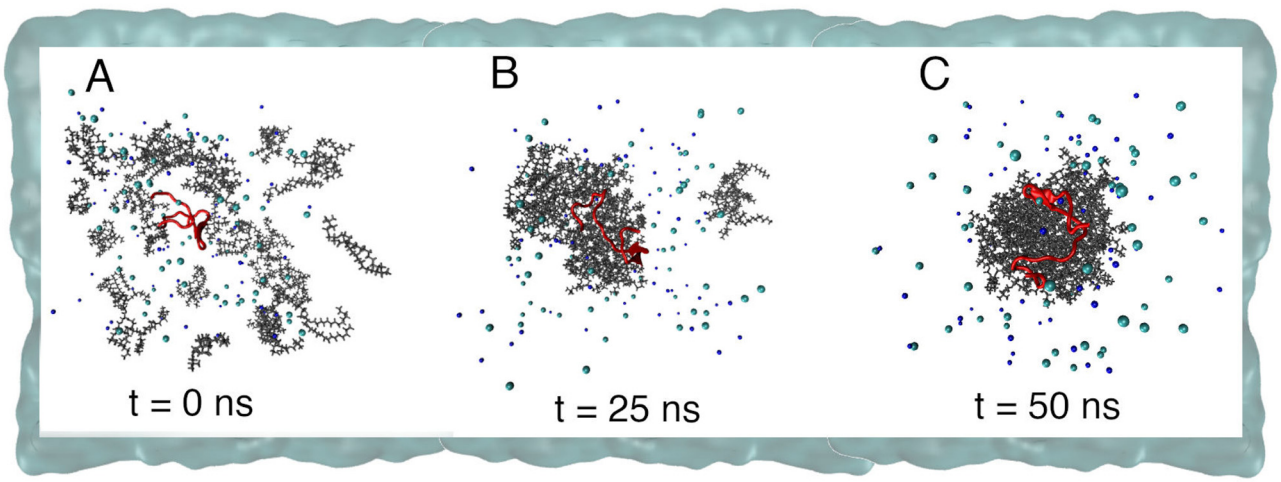

Fig. 1 Time evolution of simulations with Aβ42 (red) and 48 DMPC lipids (grey) in the presence of salt ions (blue and cyan). (A) Aβ42 monomer, lipids, and ions are initially placed randomly throughout the simulation box. (B) After 25 ns, most lipid molecules are self-assembled with Aβ42 and (C) after 50 ns, the system is fully self-assembled.

3.1 Sampling of the conformation space and convergence

Aβ42 is an IDP and as such substantial conformational fluctuations are expected to occur within each trajectory as well as among trajectories of the same set. Conformational fluctuations provide a quantitative measure of conformational space sampling whereas the time evolution of conformational dynamics offers an insight into the convergence of MD trajectories. A recent MD study of conformational dynamics of Aβ40 monomer by Paul and collaborators showed that several measures of convergence, including the secondary structure and root mean square deviations (RMSD), exhibit large fluctuations within each MD trajectory even for simulation times exceeding 10 μs.[70] The authors posed a question of whether multiple shorter trajectories (replicas) would be advantageous with regard to conformational space sampling when compared to a single, long trajectory.

We examined conformational fluctuations within each of the six sets of simulations by monitoring time evolution of the RMSD for each trajectory (Fig. S1, ESI†). Large fluctuations are observed for Aβ42 in water and water with salt in several trajectories. As lipids are added to the system, in the absence or presence of salt, fluctuations in RMSDs visibly decrease. Paul *et al.* discussed the limitations of using the RMSD as a measure of convergence and suggested using other metrics, such as the end-to-end distance or the radius of gyration, R_g.[70] In line with this discussion, we monitored time evolution of the N-to-C-terminal distance (N2CD) as displayed in Fig. S2 (ESI†). The N2CD fluctuations are larger than the RMSD fluctuations when observed within each trajectory (compare Fig. S1 and S2, ESI†). However, trajectory-to-trajectory variations of the N2CD (Fig. S2, ESI†) are significantly larger than the corresponding variations of the RMSD values (Fig. S1, ESI†). This is consistent with a rugged conformational free energy landscapes of an IDP, which can easily trap single-trajectory conformations to a local minimum.[26] Fig. S2 (ESI†) shows the N2CD averaged over 50 ns-long windows of each trajectory, followed by an average over ten trajectories (gray horizontal lines), indicating the robustness of such averages, which do not change considerably as the 50 ns window moves from 0 to 250 ns. The above observations combined indicate that multiple shorter trajectories indeed better sample the conformational space than a single albeit long trajectory, consistent with conclusions reported in earlier studies.[24,25,28] This observation has important consequences when applied to statistical analysis of MD trajectories with respect to the calculation of error bars. Trapped conformations obtained within a single MD trajectory cannot be considered statistically independent. Consequently, to ensure reliable statistical errors of the quantity of interest, the statistics should be performed over different trajectories (replicas) rather than within a single trajectory.

3.2 Comparison of MD-derived and experimental *J*-coupling constants

We here compare two sets of MD trajectories of Aβ42 monomer in pure water and in water with 150 mM NaCl to the available experimental values of *J*-coupling constants. Roche *et al.* recently reported per-residue $^3J(H^N, H^{C\alpha})$ coupling constants for both Aβ40 and Aβ42, showing that the two peptides in water, presumably under monomeric conditions at 277 K, exhibit indistinguishable values for the first 34 residues, with some differences within the C-terminal region, M35-V40.[71] We here compared the MD-derived values of $^3J(H^N, H^{C\alpha})$ for Aβ42 in pure water and in water with physiological level of salt to the experimental values of Roche and collaborators. We calculated $^3J(H^N, H^{C\alpha})$ coupling constants for each amino acid residue of an Aβ42 monomer both in pure water and water with salt using the Karplus relations.[56,72] Time averages of *J*-coupling constant values, obtained for each trajectory individually, were ensemble averaged over the respective ten trajectories and the standard error of the mean (SEM) values were calculated to reflect trajectory-to-trajectory variability.

There are several sets of Karplus parameters reported in the literature. Fig. S3 (ESI†) shows four Karplus curves for $^3J(H^N, H^{C\alpha})$ for four different sets of Karplus parameters.[57–60] The four Karplus curves in Fig. S3 (ESI†) are relatively similar to each other. Three sets of parameters: Vuister and Bax (VB) parameter set overlaps with the Hu and Bax (HB) set as well as Habeck *et al.* set within the right-handed region ($\phi < 0$) of the Ramachandran space. The VB parameter set exhibits lower values in the left-handed helical region that the other two sets, however, for residues other than glycine this region of the Ramachandran space is only sparsely populated. The parameter set of Vögeli *et al.* exhibits lower values in the vicinity of $\phi = -30^\circ$ and in the proximity of $\phi = 150^\circ$ than the other three sets.

We compared the averaging of MD-derived $^3J(H^N, H^{C\alpha})$ values over two time intervals within each trajectory: 50–250 ns and 200–250 ns. The results in Fig. S4 (ESI†) demonstrate that both choices give almost indistinguishable results, indicating that trajectory-to-trajectory variability of the *J*-coupling constant dominates over the temporal variability within an individual trajectory, as expected. We thus used the time interval 200–250 ns within each trajectory for the analysis. All MD-derived $^3J(H^N, H^{C\alpha})$ values for Aβ42 monomer in pure water and in water with salt for all four Karplus parameter sets are tabulated in Table S2 (ESI†). Table S3 (ESI†) shows the root mean square error (RMSE) calculated between MD-derived and experimental coupling constants as well as between MD-derived values calculated for Aβ42 in pure water and Aβ42 in water with salt. Notably, the differences between experimental and MD values on average surpass the differences between the two sets of MD trajectories obtained in pure water *versus* water with salt. Vögeli *et al.* Karplus parameters produce the most distinct MD-derived $^3J(H^N, H^{C\alpha})$ values between pure water and water with salt, but these differences are on average still smaller that those between experimental and MD-derived values, regardless of the solvent.

Fig. 2 shows the MD-derived *J*-coupling constant values alongside the experimental $^3J(H^N, H^{C\alpha})$ values for the HB set of Karplus parameters,[57] which produces very similar values to those based on the VB parameters[58] and parameters reported by Habeck and collaborators.[59] Fig. S5 (ESI†) shows a

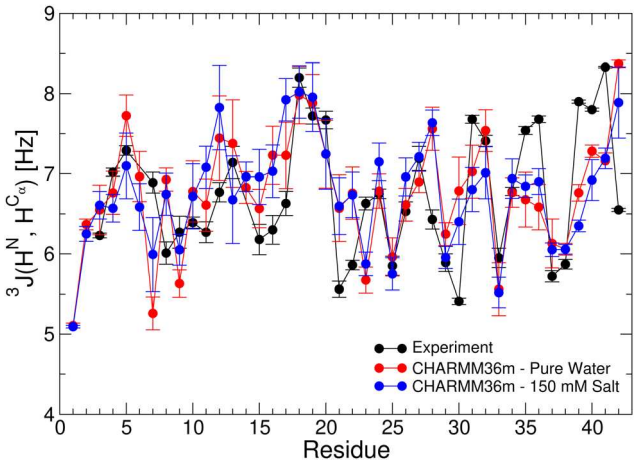

Fig. 2 $^3J(H^N, H^{C\alpha})$ coupling constants for each amino acid residue of an Aβ42 monomer from experiment[71] and calculated from MD trajectories (see Methods), using the Hu and Bax Karplus parameter set,[57] in the absence and presence of 150 mM NaCl. Error bars for MD-derived coupling constants are calculated as SEM using the averages of the corresponding set of 10 replica trajectories. Results with other Karplus parameter sets are shown in Tables S2, S3 and Fig. S5 (ESI†).

comparison of MD-derived $^3J(H^N, H^{C\alpha})$ values for all four Karplus parameter sets to the experimental data. This figure demonstrates that the Karplus parameter set of Vögeli *et al.*[60] produces MD-derived *J*-coupling constant values that deviate the most from the experimental values. Nonetheless, all four Karplus parameter sets produce MD coupling constants that are significantly lower than the experimental values for residues within the MHR and CTR: I31, M35, V36, V39, V40, I41. This result may suggest that CHARMM36m underestimates the extended β-strand conformations in this peptide region, consistent with a comparison of MD-derived and experimental $^3J(H^N, H^{C\alpha})$ coupling constants for Aβ40 reported by Paul and collaborators.[70] The opposite is true for A21, E22, and A30, for which the experimental $^3J(H^N, H^{C\alpha})$ values are lower than the MD-derived counterparts. The other deviations from the experimental data are specific to the Karplus parameter set. For example, the experimental values are lower than the MD-derived values for residues Q15, K16, and L17 for HB and Habeck Karplus parameters. Vögeli Karplus parameters produce significantly lower MD than experimental values for six hydrophobic residues in the MHR: I31-V36 and also result in underestimated MD values in the NTR at F4 and D7.

Regardless of the Karplus parameter set, $^3J(H^N, H^{C\alpha})$ values are systematically underestimated within the MHR (I31, M35, V36) and the CTR (V39, V40, I41). Our simulations were performed at 300 K, whereas the experiments were conducted at 277 K to avoid Aβ aggregation at room temperature.[71] We asked whether the differences between MD-derived and experimental per = residue *J*-coupling constants are due to this temperature mismatch. We acquired an additional set of 10 trajectories in water with 150 mM salt at 277 K and derived $^3J(H^N, H^{C\alpha})$ values using the Hu and Bax Karplus parameter set. The comparison of experimental and MD-derived values (at 277 and 300 K) is shown in Fig. S6 (ESI†). MD-derived $^3J(H^N, H^{C\alpha})$ values at 277 K show minor improvements for some amino acids (E11, E22, I32) relative to MD-derived values at 300 K but the underestimation of extended structures in the MHR and CTR remains comparable at both temperatures.

While overall CHARMM36m reproduces NMR constants fairly well, some residue-specific discrepancies are noteworthy. Alanine (A21, A30), lysines (K16, K28), and glutamic acid (E11, E22) residues, for example, all exhibit high MD-derived $^3J(H^N, H^{C\alpha})$ values, implying a significantly higher population of extended structures in MD relative to experimental values. The strong preference for the pPII structure of valine and isoleucine in CHARMM36m (and many other MD force fields), as reported in our previous work,[35] and a failure to account for the nearest neighboring effects on conformational preferences in the absence of non-local interactions[67] could explain the above observations. A similar argument can be made for aspartic acid residues. CHARMM36m as well as most other MD force fields overly promote pPII content in polar and ionizable residues at the expense of extended or turn-like structures predicted experimentally.[35] These low *J*-coupling constant values could also be explained by an increase of right-handed helical structures for these amino acid residues. However, Fig. S7 (ESI†), which shows the average per-residue coil, turn, strand, bridge, and right-handed helical content, indicates very low populations of the right-handed helical conformations. These results suggest that an overpromotion of the local pPII content for residues other than glycine, alanine, and proline, could lead to inaccuracies of MD predictions for longer IDPs, in particular because nearest neighboring interactions among residues are not sufficiently accounted for.[67]

3.3 How do salt and lipids affect the free energy landscape of Aβ42 monomers?

We here explored the effect of salt and lipids on Aβ42 free energy landscape by examining the following reaction coordinates: hydrophobic solvent accessible surface area (hydrophobic SASA), N2CD, R_g, and contact order as defined and described in Methods. Fig. 3 shows two-dimensional free energy landscapes for selected pairs of reaction coordinates for all six sets of MD trajectories.

3.3.1 Salt renders Aβ42 conformations more compact. In the absence of lipids, salt exerts significant effects on the free energy landscape of Aβ monomer. A quite rugged hydrophobic SASA *vs.* N2CD landscape with multiple comparably populated minima of Aβ42 monomer in pure water (Fig. 3(A), column 1) reduces to one global minimum in the presence of salt (Fig. 3(A), column 2). Moreover, the width of the free energy well is reduced along the N2CD coordinate as well as along the R_g coordinate upon addition of salt (Fig. 3(B), columns 1 and 2), consistent with more compact Aβ42 conformations. The free energy well in the presence of salt shifts to smaller hydrophobic SASA values, indicating that screening of charged residues by salt allows, on average, for a better hydrophobic collapse of

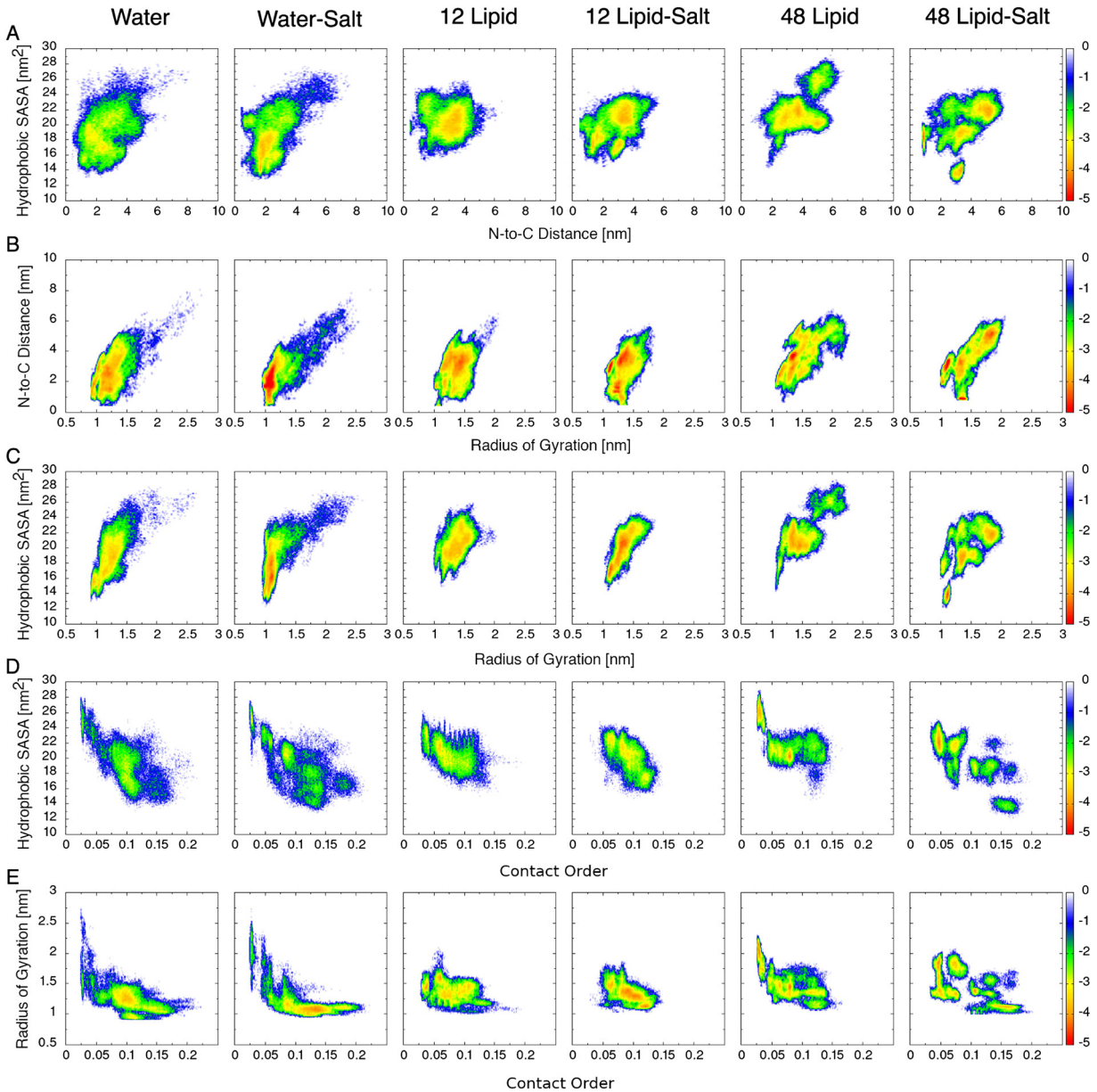

Fig. 3 Free energy landscapes of Aβ42 monomers for the following pairs of reaction coordinates: (A) hydrophobic SASA *vs.* N2CD, (B) N2CD *vs.* R_g, (C) hydrophobic SASA *vs.* R_g, (D) hydrophobic SASA *vs.* contact order, and (E) R_g *vs.* contact order. Each column corresponds to a different MD trajectory set corresponding to six different conditions under which Aβ42 conformational dynamics is examined.

Aβ42 conformations (Fig. 3(A)–(C), columns 1 and 2). Aβ42 monomer in pure water appears to be characterized by relatively uniform values of the contact order (Fig. 3(D), column 1), while in the presence of salt, the free energy landscape of hydrophobic SASA *versus* contact order displays multiple comparably populated minima along the contact order coordinate (Fig. 3(D), column 2). This comparison indicates that while salt induces Aβ42 monomer compaction, it may nonetheless increase the diversity of tertiary contacts, consistent with Aβ42 polymorphic nature. Increased compaction upon addition of salt is further supported by an increase in the average contact order as observed on the free energy R_g *vs.* contact order landscape, where the global free energy minimum shifts toward larger contact order values (Fig. 3(E), columns 1 and 2).

3.3.2 Lipids promote extended Aβ42 conformations in water without salt. The free energy landscapes of Aβ42 monomer conformations under no-salt conditions in Fig. 3(A)–(C) (columns 1, 3, and 5) demonstrate that N2CD, hydrophobic SASA, and R_g all increase with increasing lipid content. The entire distribution along the hydrophobic SASA coordinate is shifted to higher values, consistent with increased exposure of hydrophobic residues to the "solvent" (which includes water and lipids), likely due to Aβ42 interactions with lipid tails. Addition of lipids introduces significant variability in the contact order (Fig. 3(D) and (E), columns 1 and 3), suggesting significant

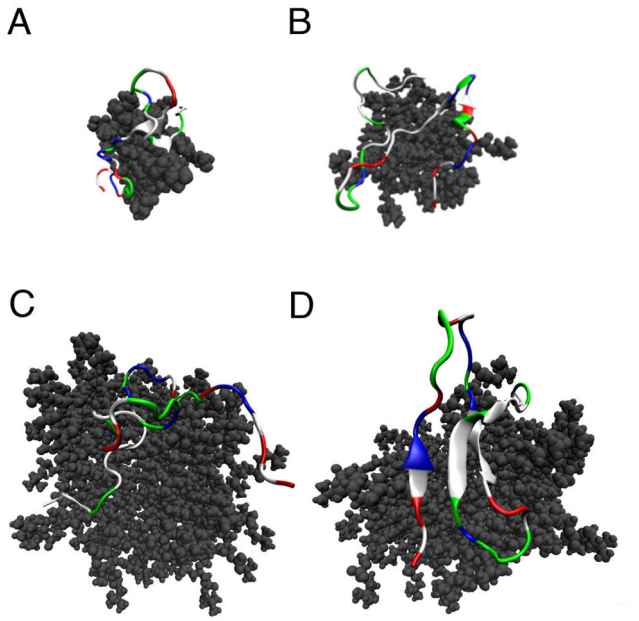

Fig. 4 Representative Aβ42 monomer conformations in the presence of (A) 12 lipids, (B) 12 lipids with salt, (C) 48 lipids, and (D) 48 lipids with salt. The visualization is produced by VMD 1.9.3 with the following color scheme: DMPC lipids are dark gray, acidic residues are red, basic residues are blue, polar residues are green, and nonpolar residues are white. The STRIDE algorithm-based secondary structure is visualized in cartoon representation. The N-terminus and C-terminus of Aβ42 can be identified by a red-white-red-white segment and a long white segment, respectively.

disruption of Aβ42 tertiary contacts due to its interaction with lipids. These observations combined indicate that DMPC lipids induces more extended and diverse Aβ42 monomer conformations in the absence of salt. To visualize Aβ42 interacting with DMPC lipids, Fig. 4(A) shows an example of Aβ42 monomer lying on and wrapping around a single cluster of 12 DMPC lipids, which provides an intuitive explanation of higher hydrophobic SASA, N2CD, and R_g values due to the presence of lipids.

Increasing lipid concentration (from 12 to 48 lipids) increases the ruggedness of the free energy landscapes of Aβ42 monomers (Fig. 3(A)–(E), columns 3 and 5). Notable are shifts to overall larger values and increased spread of N2CD, hydrophobic SASA and R_g values concomitant with an overall shift to lower contact order values (Fig. 3(A)–(E), columns 3 and 5). High hydrophobic SASA values are an expected result due to Aβ42 interactions with DMPC tails, which must disrupt and reduce tertiary Aβ42 contacts that would form in pure water. However, an increase of R_g and N2CD values indicates that DMPC lipids promote extended Aβ42 conformations. This would not be possible if Aβ42 monomer would be encapsulated within the lipid cluster. Instead, Aβ42 monomer interacts with the surface of a DMPC cluster by extending across its surface without being fully wrapped around it, as shown in Fig. 4(C). These results are consistent with previous studies that reported on an inability of Aβ monomer to penetrate a lipid bilayer made primarily of zwitterionic lipids.[22,73,74]

3.3.3 Lipids increase the ruggedness of Aβ42 free energy landscapes in water with salt. The results above show that salt (in the absence of lipids) promotes Aβ42 monomer compaction, decreases its hydrophobic SASA and increases the average and spread of the contact order values. In contrast, DMPC lipids (in the absence of salt) promote lower contact order values, larger hydrophobic SASA, and more extended Aβ42 conformations. These somewhat opposing tendencies are combined for Aβ42 in water with salt and lipids. Fig. 3 (columns 2, 4, and 6) shows the free energy landscapes of Aβ42 in 150 mM salt with 0, 12, and 48 DMPC lipids. The hydrophobic SASA *vs.* N2CD, N2CD *vs.* R_g, and hydrophobic SASA *vs.* R_g free energy landscapes, which all show unique global minima in the absence of lipids, exhibit multiple comparably populated free energy minima in the presence of lipids (Fig. 3(A)–(C), columns 2, 4, and 6). This effect is particularly strong for Aβ42 in the high lipid concentration (Fig. 3(A)–(C), column 6). Inspection of Aβ42 conformations in the presence of salt with both lipid concentrations demonstrate that Aβ42 monomer does not penetrate but rather remains at the surface of the lipid cluster, just as observed in the absence of salt. These results are consistent with previous studies which have shown that Aβ42 monomers do not embed themselves into a lipid bilayer.[22,73,74] Fig. 3 (columns 4 and 6) indicates that salt and lipids increase intrinsic disorder and conformational polymorphism of Aβ42 monomers.

3.4 How is the secondary structure of Aβ42 monomers modulated by the presence of salt and lipids?

The previous study by Voelker, Barz, and Urbanc showed that the secondary structure of Aβ40 and Aβ42 monomers through pentamers is dominated by turn and statistical coil, which together amount to over ∼90% of the secondary structure content.[29] Just like in the previous study, we here use STRIDE[62] as implemented in VMD to examine salt- and lipids-induced changes in the secondary structures of Aβ42 monomers using MD simulations with CHARMM36m.

First, we averaged the secondary structure content in each Aβ42 monomer conformation over the 42 amino acid residues and then statistically analyzed all conformations as described in Methods. The resulting analysis is shown in Table 1. The results for monomers in pure water (Table 1, row 1) which show that coil content dominates the secondary structure (≈53%) are consistent with the results reported by Voelker *et al.* who reported ≈54% coil content for Aβ42 monomers (see Table 2 in Voelker *et al.*[29]). In contrast, Table 1 (row 1) demonstrates that CHARMM36m produces significantly lower turn content (≈28%) and higher β-strand content (≈15%) than OPLS-AA/L (with 44% and 6%), respectively. Combined helical and bridge propensities in Aβ42 monomers in pure water are negligible in both CHARMM36m (≤4%) and OPLS-AA/L (≤5%). Table 1 (rows 1 and 2) demonstrates that addition of salt does not have any significant impact on the average secondary structure content of Aβ42 monomers. In the absence of salt, the helical content of Aβ42 increases only at the high lipid concentration, but remains low nonetheless.

Table 1 STRIDE-derived average secondary structure propensities of Aβ42 monomers for the six different conditions under study

Salt [mM]	# Lipids	Coil	Turn	β-Strand	Helix	Bridge
0	0	0.53 ± 0.03	0.28 ± 0.02	0.15 ± 0.02	0.01 ± 0.01	0.03 0.01
150	0	0.52 ± 0.03	0.29 ± 0.02	0.13 ± 0.02	0.01 ± 0.01	0.04 0.01
0	12	0.55 ± 0.03	0.31 ± 0.03	0.10 ± 0.02	0.01 ± 0.01	0.02 0.01
150	12	0.47 ± 0.03	0.36 ± 0.02	0.12 ± 0.02	0.00 ± 0.00	0.04 0.01
0	48	0.57 ± 0.03	0.30 ± 0.03	0.05 ± 0.01	0.04 ± 0.01	0.02 0.01
150	48	0.47 ± 0.03	0.36 ± 0.03	0.13 ± 0.02	0.00 ± 0.00	0.03 0.01

Table 2 The average SASA and interface area alongside SEM values as derived for Aβ42 monomer, DMPC cluster, Aβ42–DMPC complex, and the interface area between the protein and lipid cluster

Salt [mM]	# Lipids	⟨Area⟩ [nm^2]	SEM
Aβ42 monomer SASA			
0	0	44.08	1.30
150	0	43.07	1.54
0	12	46.72	0.86
150	12	44.87	1.21
0	48	47.87	1.18
150	48	45.30	1.36
DMPC cluster SASA			
0	12	66.15	0.72
150	12	66.31	0.71
0	48	204.07	4.96
150	48	203.73	5.92
Aβ42–DMPC cluster SASA			
0	12	90.33	1.12
150	12	89.88	1.29
0	48	220.92	5.38
150	48	218.99	5.89
Aβ42–DMPC interface area			
0	12	11.27	0.63
150	12	10.65	0.64
0	48	15.51	0.93
150	48	15.01	1.01

Increasing lipid concentration in the absence of salt (Table 1 rows 1, 3, and 5) results in a minor increase in overall coil content (from 53% to 57%), similar turn content, and a significant decrease in β-strand content (from 15% to 5%). However, increasing lipid concentration in the presence of salt (Table 1 rows 2, 4, and 6) has the opposite effect on the overall secondary structure of Aβ42 monomer. Although not statistically significant, coil content decreases from 52% to 47%. Turn content increases from 29% to 36% for both lipid concentrations, consistent with findings reported by Fatafta *et al.*[22]

In the following, we asked if the secondary structure propensities of specific Aβ42 regions may be affected by the presence of salt and/or lipids. Fig. S7 (ESI†) shows per-residue propensities for each of the five secondary structure elements of Aβ42 monomer for each of the six different solvent conditions. To facilitate comparisons, Fig. 5 shows the average per-residue coil, β-strand, and turn propensities without (panels A–C) and with salt (D–F) for three lipid concentrations under study (see Methods). To better grasp the effect of salt addition to Aβ42 interacting with lipids at the three concentrations, we also plot differences caused by addition of salt in panels G–I of Fig. 5. Note that the error bars are quite large because they reflect the trajectory-to-trajectory variability. If the error bars were derived from time averaging of propensities within individual trajectories, they would be negligibly small. Hence, the error bars are likely overestimated in Fig. 5.

3.4.1 Salt reduces coil propensities in the CHC, MHR, and CTR of Aβ42 interacting with lipids at the high lipid concentration. Panels A, D, and G of Fig. 5 show the effect of lipids and salt on per-residue coil propensities of Aβ42 monomers. In the absence of lipids, per-residue coil propensities of Aβ2 are, on average, not strongly affected by salt (Fig. 5(G) black curve). When Aβ42 interacts with lipids at the low or high lipid concentration under no salt conditions, lipids induce minor changes in per-residue coil propensities (Fig. 5(A), green curve).

In the presence of salt, the effect of lipids on per-residue coil propensities depends on the lipid concentration. At a low lipid concentration, coil propensities only slightly increase at K16, V18, N27-K28 and V40-I41 and more prominently decrease at A2 and in the R5-G9, V12-H14, F19-F20, D23-S26 regions (Fig. 5(B), green curve). At the high lipid concentration, coil propensities mostly only decrease in the V18-F20, G25-S26, I31-L34, V36-V40 regions with minor increases in the NTR (Fig. 5(D), red curve). Thus, in the presence of salt, the low lipid concentration reduces per-residue coil propensities more in the NTR of Aβ42, whereas the high lipid concentration reduces coil propensities more in the MHR and CTR of Aβ42. Notably, both low and high lipid concentrations reduce the coil propensities within the CFR of Aβ42, rendering this region more structured.

The effect of salt addition on per-residue coil propensities is examined in Fig. 5(G). When Aβ 42 interacts with lipids at the low lipid concentration, addition of salt decreases coil propensities along most of the sequence (Fig. 5(G), green curve). Adding salt to Aβ42 interacting with lipids at the high lipid concentration results in a substantial decrease of coil propensities along most of the sequence (Fig. 5(G), red curve).

3.4.2 Salt restores β-strand propensities within the CHC, MHR, and CTR of Aβ42 interacting with lipids. Fig. 5(B), (E) and (H) shows the effect of salt and lipids on per-residue β-strand propensities in Aβ42 monomers. In the absence of lipids, added salt overall decreases β-strand propensities (Fig. 5(H), black curve). In the absence of salt, lipids affect β-strand propensities in the lipid concentration-dependent way. At the low lipid concentration under no-salt conditions, β-strand propensities significantly decrease (Fig. 5(B), green curve). At the high lipid concentration in the absence of salt, β-strand propensities decrease further along the entire Aβ42 sequence (Fig. 5(B), red curve).

In the presence of salt, addition of lipids imparts smaller effects on per-residue β-strand propensities of Aβ42 than under

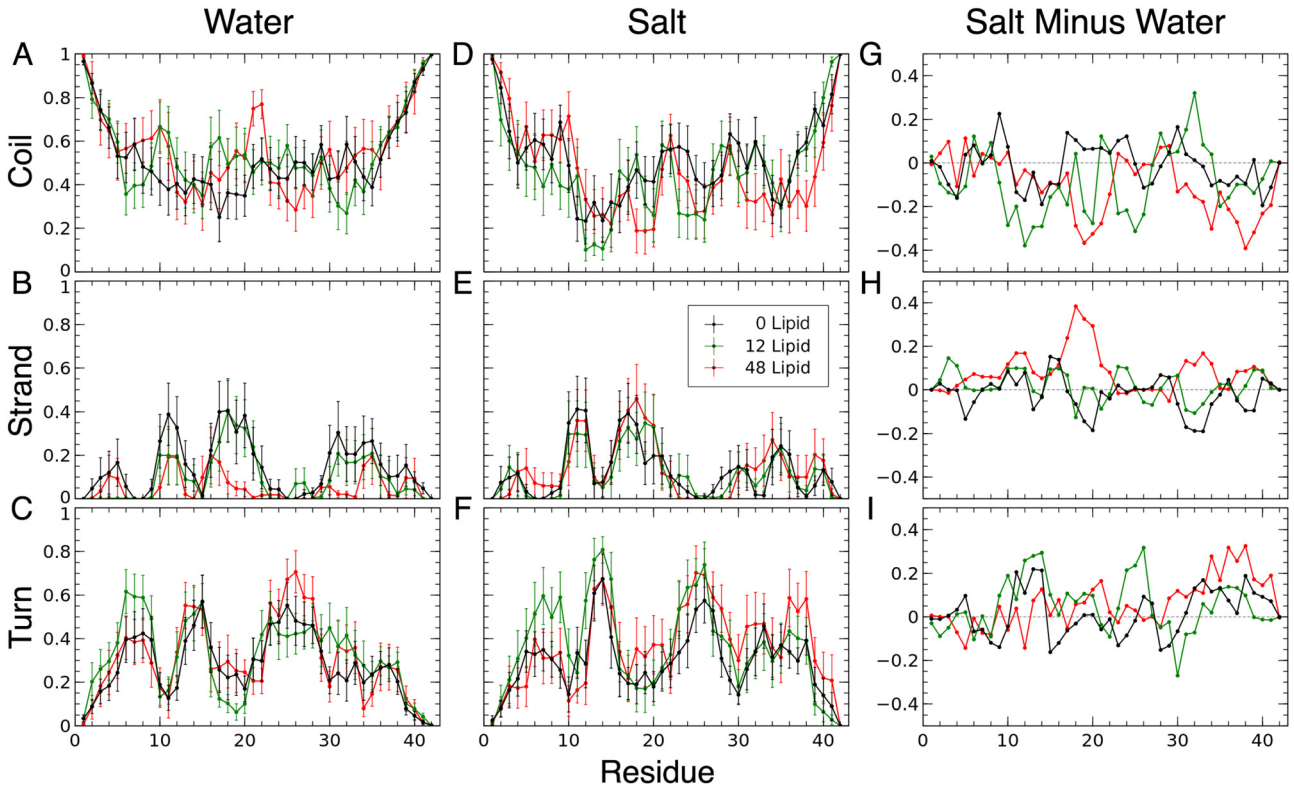

Fig. 5 STRIDE-based per-residue coil, β-strand, and turn secondary structure propensities of Aβ 42 monomer in the presence of 0, 12, and 48 DMPC molecules (0, 27, and 109 mM) in (A)–(C) pure water and (D)–(F) water with 150 mM NaCl. (G)–(I) Propensity differences between water with salt and water without salt are shown for three DMPC concentrations. Error bars correspond to SEM values and reflect trajectory-to-trajectory variability as described in Methods.

no-salt conditions (Fig. 5(E)). Under salt conditions, addition of lipids at the low lipid concentration has a minor residue-specific effect on β-strand propensities of Aβ42 conformations (Fig. 5(E), green curve). In comparison, adding the high lipid concentration to Aβ42 in water with salt increases β-strand propensities back to the level observed in pure water (Fig. 5(E), red curve).

The effect of salt can be observed in Fig. 5(H). When Aβ42 is interacting with lipids at the low lipid concentration, the addition of salt slightly increases β-strand propensities along most of the sequence in the A2-F4, Y10-V12, Q15-L17, D23-V24, G29-A30, V39-V40 regions and decreases these propensities in at V18, A21 and in the S26-N27, I31-G33 regions (Fig. 5(H), green curve). When Aβ42 is interacting with lipids at the high lipid concentration, salt significantly increases β-strand propensities along the entire Aβ42 sequence (Fig. 5(H), red curve). This increase in β-strand propensities is particularly large within the MHR and CTR. It is worth noting that per-residue coil propensities significantly decreases in these two regions due to addition of salt at the high lipid concentration (Fig. 5(G), red curve), so these two changes are concomitant. These results elucidate the important role of salt in maintaining the β-strand content of Aβ42 interacting with lipids within the hydrophobic regions of this peptide, which are associated with amyloid formation.

3.4.3 Lipids stabilizes the turn in the CFR of Aβ42. Fig. 5(C), (F) and (I) shows the effect of salt and lipids on per-residue turn propensities in Aβ42 monomers. In the absence of lipids, addition of salt results in minor changes in turn propensities (Fig. 5(I), black curve). In the absence of salt, adding lipids at the low lipid concentration increases per-residue turn propensities of Aβ42 in the NTR and at A30, while slightly decreasing these propensities in the CHC region (Fig. 5(C), green curve). When lipids are added to pure water at the high lipid concentration, per-residue turn propensities increase in the CFR and MHR (Fig. 5(C), red curve). The increase in turn propensities within the CFR at the high lipid concentration implies that in the absence of salt, lipids stabilize the CFR of Aβ42.

In the presence of salt, addition of lipids at both low and high concentrations results in an overall increase of per-residue turn propensities, however, the affected regions are lipid-concentration specific (Fig. 5(F)). Lipids at the low lipid concentration increase turn propensities predominantly in the first half of the sequence (Fig. 5(F), green curve). Lipids at the high lipid concentration, in comparison, increase turn propensities in the CHC, CFR, MHR, and CTR (Fig. 5(F), red curve). Both lipid concentrations increase turn propensities within the CFR in the presence of salt. Combined with the above observations, we conclude that lipids stabilize the turn within the CFR of Aβ42, regardless of the absence/presence of salt.

The effect of salt on Aβ42 at the low and high lipid concentrations can best be examined by inspecting water with salt to water without salt turn propensity differences shown in Fig. 5(I) (green and red curves). When Aβ42 is interacting with lipids at the low lipid concentration, addition of 150 mM salt

results in increased per-residue turn propensities in the CHC, CFR, and CTR with a decrease in the I31-G33 Fig. 5(I) (green curve). When Aβ42 interacts with lipids at the high lipid concentration, adding 150 mM salt results in increased per-residue turn propensities in the CHC, MHR, and CTR (this latter region being the most affected) Fig. 5(I) (red curve). Addition of salt to Aβ42 interacting with lipids at the high lipid concentration stabilizes the turn at the CTR.

The secondary structure analysis described above shows that the effect of lipids on the secondary structure of Aβ42 depends on the lipid concentration, while salt modulates specific per-residue secondary structure propensities of Aβ42 interacting with DMPC lipids. Fig. 4 provides important insights into these effects by showing the extraordinary ability of Aβ42 to wrap itself around self-assembled lipids without immersing itself into the lipid self-assembly. The low lipid concentration leads to Aβ42 monomer adhered to a small quasi-spherical 12-lipid cluster (Fig. 4(A) and (B)), thereby enhancing turn propensities in Aβ42 conformations, particularly in the N-terminal half of the sequence. At the high lipid concentration, a larger quasi-spherical lipid cluster is formed, which allows Aβ42 monomer to ''flatten'' on its surface and adopt a more extended structure, which in the presence of salt leads to enhanced β-strand content (Fig. 4(C) and (D)).

3.5 How do salt and lipids affect the tertiary structure of Aβ42 monomer conformations?

Due to its intrinsically disordered nature, Aβ42 monomer is not expected to make unique and stable tertiary contacts. Nonetheless, the frequency or probability of intramolecular contact formation provides valuable information about the conformational dynamics of this peptide. For each of the six sets of MD trajectories, we calculated tertiary contact probabilities as described in Methods, which are displayed as contact maps in Fig. 6(A). To better facilitate pair-wise comparisons among these tertiary contacts of Aβ42 under six different conditions, Fig. 6(B)–(F) shows pair-wise contact map differences, which are obtained by subtracting the reference contact map denoted by 'X' from the contact map in the respective column.

3.5.1 Salt facilitates formation of long-range tertiary contacts in Aβ42. Fig. 6(B) shows differences in tertiary contact probabilities for five conditions that contain 150 mM salt, the low lipid concentration without and with salt, and the high lipid concentration without and with salt. In pure water, Aβ42 forms four groups of contacts (loops) along the sequence between the following pairs of regions: D1-H6/S8-Q15, E11-K16/H14-G25, K16-G25/S26-A42, and S26-G33/L34-A42, of which the third loop involves the CFR stabilized by contacts between CHC and MHR (Fig. 6(A), column 1). Particularly interesting are the long-range contacts of F4 and V12 with MHR (F4/MHR and V12/MHR). Upon addition of salt in the absence of lipids, the D1-H6/S8-Q15 loop unfolds, enabling the A2-F4 region to form a long-range tertiary contacts with the N27-G38 region and V12 to form long-range tertiary contacts with the CTR (Fig. 6(A) and (B), column 2). Concomitantly, the second group of contacts is enhanced and the third one diminished. Thus, salt induces formation of long-range tertiary contacts in Aβ42 monomers, rendering the conformations more compact.

3.5.2 Low lipid concentration causes partial Aβ42 unfolding in the absence of salt whereas salt addition facilitates formation of new tertiary contacts. In the presence of the low lipid concentration in no-salt conditions, the first and the fourth loop of contacts (D1-H6/S8-Q15 and S26-G33/L34-A42) unfold while the long-range contacts F4/MHR and V12/MHR are diminished in favor of interactions between H6 and the MHR (Fig. 6(A) and (B), column 3). Adding salt to Aβ42 at the low lipid concentration results in tertiary contacts between the A2-H6 region and the V18–S26 region, which are not observed under any other conditions (Fig. 6(A) and (D), column 4). Concomitantly, the second and third loops of contacts (E11-K16/H14-G25, K16-G25/S26-A42) are enhanced and the fourth loop of contacts (S26-G33/L34-A42), observed in pure water, is restored when salt is added. In the presence of salt, addition of the low lipid concentration to Aβ42 monomer results in diminished long-range tertiary contacts between the A2-F4 and the MHR whereas the contacts between A2-F4 and the CFR are enhanced (Fig. 6(A) and (C), column 4).

3.5.3 High lipid concentration causes significant Aβ42 unfolding in the absence of salt and addition of lipids to Aβ42 in water with salt destabilizes tertiary contacts of the NTR with other peptide regions. When Aβ42 interacts with lipids at the high lipid concentration in the absence of salt, most tertiary contacts resemble those observed for Aβ42 monomer in pure water, however, the contacts are visibly fewer and significantly weaker (compare Fig. 6(A) and (B), column 5). This observation of lipid concentration-dependent Aβ42 tertiary structure disruption is consistent with increased coil and decreased β-strand propensities (Table 1). Under no-salt conditions, addition of the high concentration of lipids causes inhibition of the V12/MHR contacts and the A2-F4 region interacts with the A30-I32 region rather than with the L34-V36 region (Fig. 6(A) and (B), column 5). When salt is added to Aβ42 interacting with lipids at the high lipid concentration, tertiary contacts are enhanced within the second and third loops of contacts (E11-K16/H14-G25 and K16-G25/S26-A42), while the contacts within the first loop (D1-H6/S8-Q15) become weaker (Fig. 6(A) and (F), column 6). When lipids are added to Aβ42 monomer in water with salt, Aβ42–lipid interactions modify tertiary contacts involving NTR and CFR without exerting major changes (Fig. 6(A), columns 2,4,6; Fig. 6(C), columns 4,6 and Fig. 6(E), column 6).

3.5.4 Salt and the high concentration of lipids induce formation of a parallel β-strand in Aβ42 conformations. Fig. 6(F) shows the effect of salt on Aβ42 interacting with lipids at the high lipid concentration (column 6). The effect of increasing the lipid concentration on the tertiary structure of Aβ42 in the presence of salt is displayed in Fig. 6(E) (column 6). In both difference maps, we observe strong contacts between the F4-D7 and N27-I32 regions. Thus, the combination of the salt and high lipid concentration promotes formation of these contacts associated with a parallel β-strand structure (Fig. 6(A), column 6). The strength of contacts between the F4-D7 and

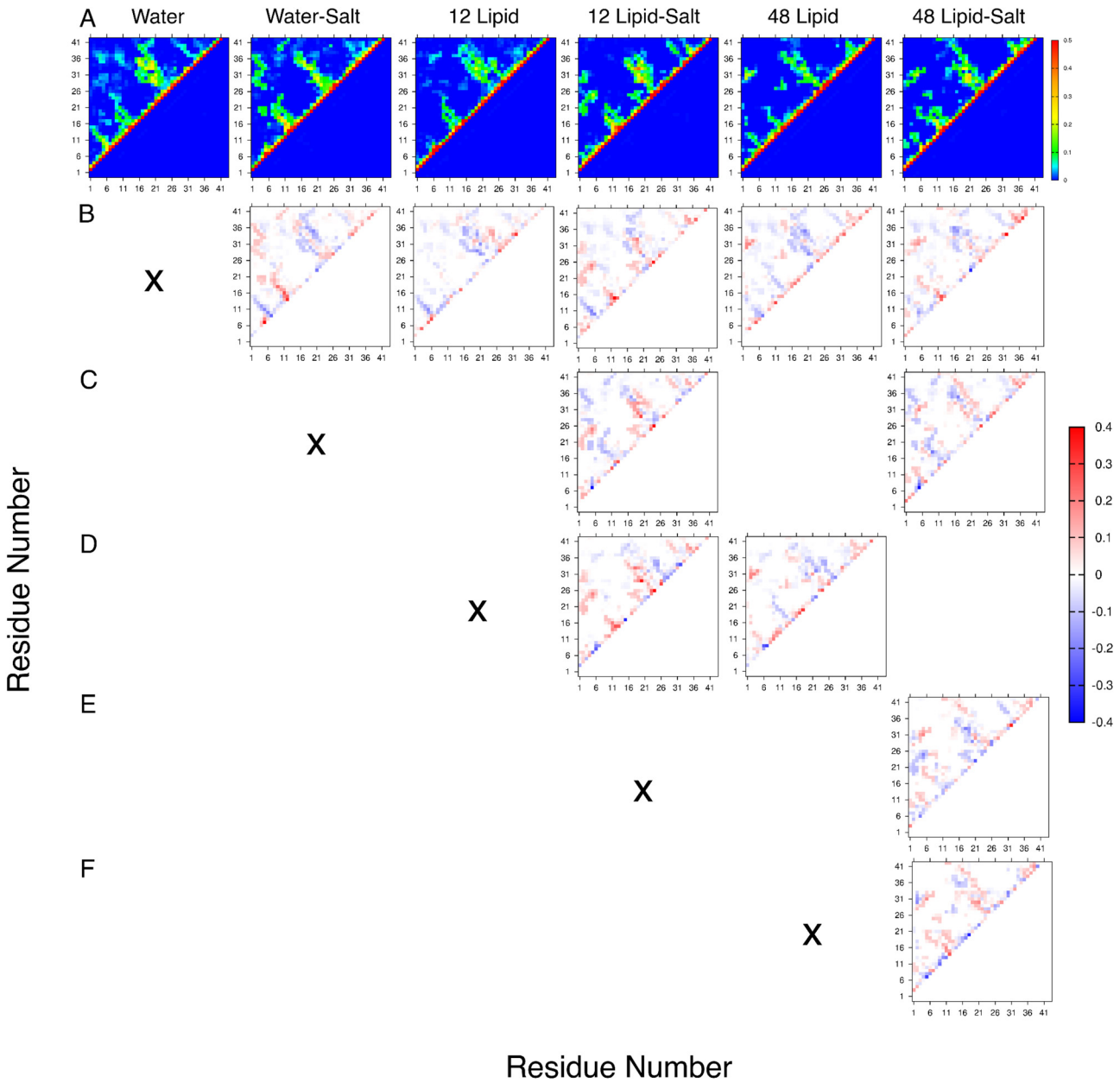

Fig. 6 (A) Tertiary contact maps of Aβ42, showing the probability (color bar) that pairs of C_α atoms are within a distance of 6 Å for each of the six different conditions under study. (B)–(F) Pairwise difference contact maps indicating stronger (red) and weaker (blue) contacts relative to the reference contact map indicated by X.

I31-32 regions in conditions with salt and 48 lipids relative to the other five conditions (Fig. 6(B)–(F), column 6) implies that this parallel β-strand results from a cooperative effect of Aβ42–salt and Aβ42–lipid interactions.

3.6 How is the average per-residue distance of Aβ42 to lipid head and tail groups affected by salt and lipid concentration?

To gain insight into Aβ42–lipid interactions, we study the average minimum distance of each amino acid residue to three different types of atoms of DMPC lipids: the N-atom of the head group, the P-atom of the head group, and any C-atom of the two tails (Fig. S8, ESI†) (see Methods).

3.6.1 Aβ42–lipid interactions are driven by hydrophobic residues interacting with lipid tail groups. Fig. 7 shows the resulting average minimum distance between the amino acid residues of Aβ42 to the proximate N-atoms, P-atoms, and tail C-atoms of DMPC molecules in the absence and presence of salt at the two lipid concentrations. Regardless of the presence of salt at both lipid concentrations, the minimal distance of any residue to the N-atom is almost the same as the minimal distance to the P-atom of DMPC lipids (Fig. 7, black *vs.* red curves). There are some exceptions to this observation, for example, several residues in the CHC and MHR are closer to the P-atoms than to the N-atoms, but the average value

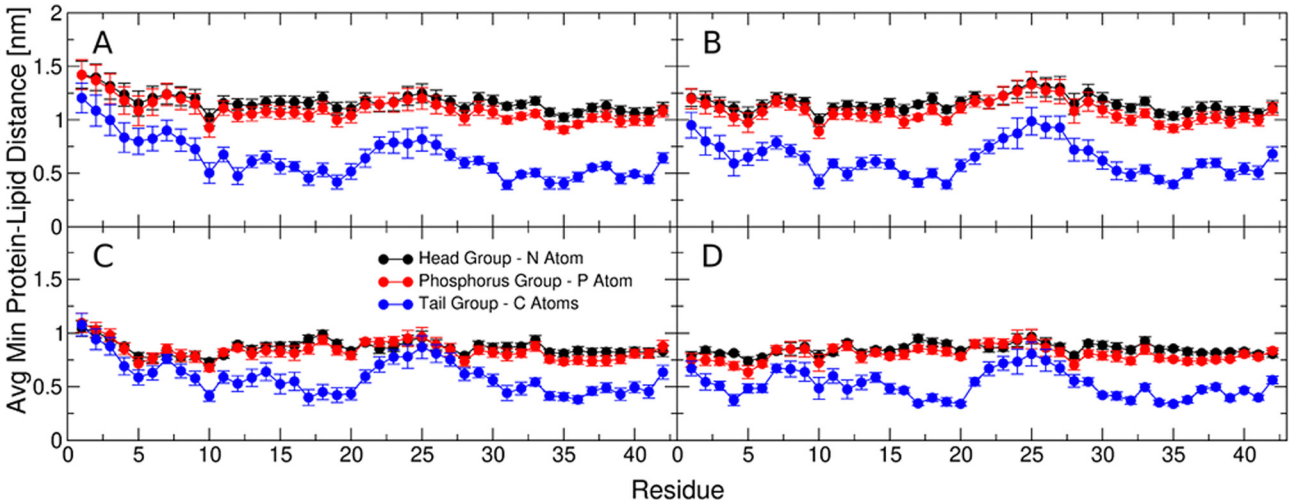

Fig. 7 A minimum average distance between Aβ42 residues and DMPC head groups, the N atom (black) and the P atom (red), and any carbon atom of DMPC tails (blue) for the following conditions: (A) 12 lipids and pure water, (B) 12 lipids and 150 mM salt, (C) 48 lipids and pure water, and (D) 48 lipids and 150 mM salt. For each of the four conditions, the averages are calculated using 50–250 ns of the respective 10 replica trajectories and error bars are calculated as SEM values reflecting trajectory-to-trajectory variability.

differences never exceeds 2–3 Å. SEM values give an indication of which regions of the protein are involved in transient or more stable intermolecular interactions with the lipid molecules. Both in the absence and presence of salt, all amino acid residues are closer to the C-atoms of DMPC tails than to N- and P-atoms of DMPC heads ($\lesssim$10 Å). Overall, regardless of the absence or presence of salt, SEM values for the NTR and CFR distances are larger ($\approx$1–1.5 Å), indicating more transient interactions, whereas SEM values for the CHC, MHR, and CTR distances are smaller ($\approx$0.3–0.9 Å), indicating less fluctuations and thus more stable protein–lipid contacts.

3.6.2 Salt induces interactions between the NTR of Aβ42 and lipids and moves the CFR of Aβ42 away from lipids at the low lipid concentration. Fig. 7(A) and (B) shows the average minimum Aβ42–lipid distances for the low lipid concentration in pure water and water with 150 mM salt, respectively. Although the NTR and CFR are not as close to the lipid tail groups as the hydrophobic Aβ42 regions, they are nonetheless closer to the lipid tail groups than to the N- and P-atoms of DMPC lipids. The two regions react slightly differently to the introduction of salt. Addition of salt results in the NTR moving closer to and the CFR moving further away from the DMPC tail groups. A more direct investigation of the influence of the salt concentration on protein interactions with 12 lipids can be achieved by examining the differences in the minimum average protein–lipid distances. Fig. S9A (ESI†) demonstrates the result of subtracting the distances in Fig. 7(B) from those in Fig. 7(A). A negative value indicates that the amino acid residue is closer to the respective lipid group in the presence of salt than in pure water at the low lipid concentration. These results imply that salt allows the NTR to better interact with DMPC molecules.

3.6.3 Addition of salt at the high lipid concentration facilitates interactions between the NTR of Aβ42 and lipids. Fig. 7(C) and (D) shows the average minimum distance between the protein and different lipid atoms at the higher lipid concentration. Differences between the distances of any amino acid residue and the head or tail groups of the lipid are noticeably smaller than for the low lipid concentration and particularly so in the NTR and CFR of Aβ42. Fig. S9B (ESI†) demonstrates the result of subtracting the distances in Fig. 7(D) from those in Fig. 7(C) and, therefore, the changes of protein–lipid interactions when salt is introduced at the high lipid concentration. As observed at the low lipid concentration, addition of salt results in the NTR moving significantly closer to all three atom types of DMPC lipids. It is worth noting that these residues are involved in the formation of the parallel β-strand visualized in Fig. 4, which forms only in the presence of salt at the high lipid concentration. In contrast to the low lipid concentration, addition of salt at the high lipid concentration does not affect the Aβ42–lipid distances in the CFR (Fig. S9B, ESI†).

3.6.4 The NTR of Aβ42 moves closer to the lipid heads as the lipid concentration increases in water without salt. The effect of the lipid concentration on Aβ42–lipid interactions in the absence of salt can be observed in Fig. S9C (ESI†). Fig. S9C (ESI†), which is the result of subtracting Fig. 7(C) from Fig. 7(A), compares the average minimum distance in pure water at the low and high lipid concentrations. At the high lipid concentration (when compared to the low lipid concentration), the average minimum distance between the NTR and lipid head N- and P-atoms decreases by $\approx$4 Å, whereas for all other amino acid residues this decrease is somewhat smaller, $\approx$2–3 Å. Upon the increase of the lipid concentration, the minimum distances of the NTR and the V36-G38 region to the C-atoms of DMPC lipids also decrease, but these distances are affected less than the distances between Aβ42 and the two head group atoms.

3.6.5 Salt facilitates the proximity of Aβ42 to lipids at the high lipid concentration. Fig. S9D (ESI†) shows the high to low

lipid concentration difference in the minimum distance between each amino acid residue of Aβ42 and lipid atoms in the presence of salt. These results show that at the high lipid concentration the average distance between the NTR (with an exception of Y10) and the P-, N-, and C-atoms of DMPC lipids is even smaller than at the low lipid concentration in the presence of salt. Additionally, the CFR is significantly closer to the N- and P-atoms of the DMPC lipids when salt is present. In particular, A20 and the G25-A30 region are significantly closer ($\approx$2 Å) to the carbon tail groups upon increased lipid concentration. The high lipid concentration in the presence of salt produces the most significant decrease in the average minimum Aβ42–lipid distances, thereby allowing for the most prominent interactions between the peptide and lipids. Regardless of the presence or absence of salt, the two hydrophobic peptide regions with the smallest average minimal distance to lipid tail groups are L17-A20 and L34-V36. However, in the presence of salt, which allows the NTR to interact with lipids more avidly, the average minimal distance of F4 to lipid tail groups becomes comparable to the respective distances of the L17-A30 and L34-V36 regions (Fig. 7(D)).

3.7 Aβ42–lipid interface area increases with the lipid concentration but does not exceed a third of the accessible surface area of Aβ42

To further elucidate the interactions between Aβ42 and DMPC lipids, we derive distributions of SASA values of Aβ42, the DMPC cluster, and the Aβ42–DMPC complex, as implemented in VMD. The interface area between Aβ42 and DMPC cluster can be calculated from the above SASA values (see Methods). The effect of salt and lipid concentration on this interface area provides additional insights into protein–lipid interactions, whereby a larger interface area would indicate stronger Aβ42–lipid association. The results of these calculations are displayed in Fig. 8 and Fig. S10 (ESI†). To verify that the lipids in complex with Aβ42 remain self-associated in a single cluster, Fig. S11 (ESI†) shows an average size distribution of DMPC molecules (see Methods for details) at both lipid concentrations in the absence and presence of salt. These size distributions showcase the stability of DMPC clusters by revealing a single peak at 12 or 48 at the low and high lipid concentrations, respectively, with almost exclusively zero error bars. Only in the case of the high lipid concentration in water with salt, there is an instance of the cluster of 48 DMPC molecules separating into a two clusters (with 34 and 14 lipids), but this event does not affect the size distribution in a statistically significant way, demonstrating that Aβ42–lipid complexes are stable both for 12 and 48 lipids.

Fig. 8(A) shows the SASA distribution of Aβ42 for all six sets of MD trajectories. In the absence of lipids, the solvent comprises either pure water or water with salt (gray and brown curves). When Aβ42 interacts with lipids, the solvent in the calculation of the corresponding SASA values comprises of water, salt, and lipids. Fig. 8(A) shows the SASA distribution of Aβ42 interacting with lipids at the low and high lipid concentrations in the absence and presence of salt (black, red, green, and blue curves). To better visualize the effects of salt and lipids on SASA distributions, Fig. S10 (ESI†) displays

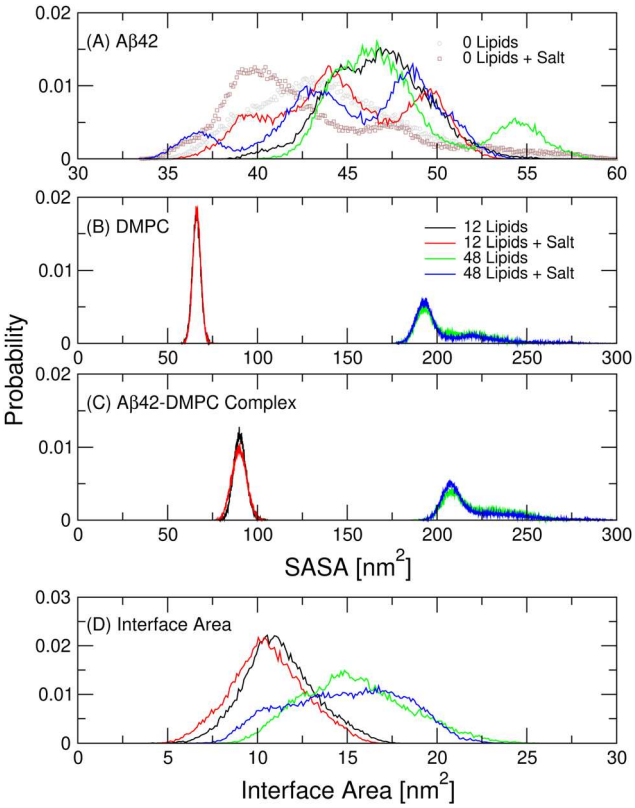

Fig. 8 Normalized distributions of the SASA of (A) Aβ42 monomer, (B) DMPC cluster, (C) Aβ42–DMPC complex, and (D) the interface area between Aβ42 and the DMPC cluster, as described in Methods. Additional distributions of the SASA values of Aβ42 in the absence of lipids are included in panel (A) for reference and are also displayed in Fig. S10 (ESI†) to facilitate a better comparison among the distributions.

the SASA distributions of the Aβ42 monomer in Fig. 8(A) separately for pure water (Fig. S10A, ESI†) and water with 150 mM NaCl (Fig. S10B, ESI†).

Fig. 8(A) and Fig. S10 (ESI†) (black curves) demonstrate that the SASA distribution of the Aβ42 monomer in pure water with no lipids is unimodal with a peak at 43 nm^2. In the presence of salt, the SASA distribution becomes bimodal with the most prominent peak at 39 nm^2 and a smaller peak at 42 nm^2, indicating a decrease of average monomer SASA (Fig. 8(A), grey circles *vs.* brown squares and Fig. S10A and B (ESI†), black curves), consistent with salt-induce partial hydrophobic collapse of Aβ42 conformations. In the low lipid concentration in the absence of salt, a single peak at 47 nm^2 (Fig. 8(A) black curve and Fig. S10A, ESI† red curve) is observed, whereas addition of salt induces a trimodal SASA distribution with peaks at 39, 44, and 50 nm^2 (Fig. 8(A), red curve and Fig. S10B, ESI† red curve), indicating that salt increases polymorphism of Aβ42 conformations. When Aβ42 interacts with lipids at the high lipid concentration in the absence of salt, the SASA distribution changes from a unimodal (at the low lipid concentration) to a bimodal distribution with peaks at 46 and 54 nm^2 (at the high lipid concentration), thereby increasing the average SASA of Aβ42 (Fig. 8(A), green curve and Fig. S10A, ESI†

green curve). This shift to larger SASA values is due to a partial Aβ42 unfolding concomitant with enhanced contacts between Aβ42 and lipids (Fig. 8(A), green curve). Adding salt to Aβ42 in water with the high lipid concentration renders the SASA distribution trimodal with peaks at 37, 43, and 48 nm^2 while shifting the average to a lower value (Fig. 8(A), blue curve and Fig. S10B (ESI†), green curve). Hence, salt, on average, decreases Aβ42 SASA values and introduces multiple maxima in the SASA distribution, increasing the degree of intrinsic disorder in Aβ42 conformations, consistent with salt-induced changes in the free energy landscapes in Fig. 3.

Fig. 8(B) shows the SASA distribution of lipid clusters at the low and high lipid concentrations in the absence and presence of salt. Note that the solvent in this SASA calculation comprises of water, salt, and Aβ42. Both in the absence and presence of salt, the SASA distributions at the low lipid concentration are unimodal with a peak at 66 nm^2 and overlap each other (black and red curves). Similarly, salt does not considerably affect the SASA distribution of lipids at the high lipid concentration with a dominating peak at 192 nm^2 (green and blue curves). Interestingly, the SASA distribution at the high lipid concentration (regardless of the presence or absence of salt) slightly deviates from a unimodal distribution and shows an additional albeit lowly populated peak at 210 nm^2. This deviation from unimodality indicates that at the high lipid concentration, the lipid cluster adopts more flexible structure than the cluster formed at the low lipid concentration.

Fig. 8(C) shows the SASA distribution of Aβ42–DMPC complex at the low and high lipid concentrations in the absence and presence of salt. The solvent in this SASA calculation comprises of water and salt. These distributions highly resemble those in Fig. 8(B), however, they are shifted to higher SASA values, such that at the low lipid concentration the peak of the unimodal SASA distribution is at 89 nm^2, whereas at the high lipid concentration the dominant peak is at 208 nm^2 with the second lowly populated peak at 225 nm^2. Clearly, the average SASA of the Aβ42–DMPC complex is significantly smaller than the sum of the average SASA values of Aβ42 alone and the lipid cluster alone.

The difference between the sum of SASA values of Aβ42 alone and DMPC cluster alone and the SASA of the Aβ42–DMPC complexed, divided by two, corresponds to the interface area between Aβ42 and the lipid cluster, displayed in Fig. 8(D). At the low lipid concentration, the interface area distribution is unimodal with average and SEM values of 11.27 ± 0.63 nm^2 and 10.65 ± 0.64 nm^2 in the absence and presence of salt, respectively (black and red curves). This result shows that salt decreases the Aβ42–DMPC interface area. This is consistent with increased compaction of Aβ42 fold due to increased tertiary contacts. At the high lipid concentration, the interface area distribution is shifted to higher values and significantly increases in width, as indicated by the increased averages and SEM: 15.51 ± 0.93 nm^2 and 15.01 ± 1.02 nm^2 in the absence and presence of salt, respectively (green and blue curves). These results show that at the high lipid concentration Aβ42 interacts more strongly with lipids than at the low lipid concentration. We then ask what fraction of the total Aβ42 SASA is in contact with lipids. If this fraction was close to 1, this would indicate that the entire Aβ42 monomer is embedded into the lipid cluster. The results in Fig. 8 clearly show that this is not the case. If we compare the average interface area to the average SASA of Aβ42 in pure water or pure water with salt, we can see that even at the high lipid concentration the ratio of the interface area to the SASA of Aβ42 remains rather low, 33%, demonstrating that Aβ42 monomer indeed interacts with the surface rather than getting embedded into the DMPC cluster.

4 Conclusions and discussion

Due to its strong association with AD, Aβ42 is currently one of the most widely investigated IDPs. In particular, Aβ42 interaction with free lipids have recently garnered attention.[20–22] In this MD study, we ask how a physiological level of salt affects the conformational ensemble of Aβ42 and study the effects of different lipid concentrations on conformational dynamics of this IDP in the absence and presence of salt. We conducted extensive MD simulations for six different types of systems (Aβ42 in water with 0, 12, and 48 DMPC lipids in the absence and presence of 150 mM NaCl at 300 K) with ten 250 ns-long replica trajectories for each type. To facilitate a comparison to per-residue experimental *J*-coupling constants, additional ten 250 ns-long trajectories were acquired at 277 K with a total simulation time of 17.5 μs. We monitored the time evolution of the RMSD and N2CD values of Aβ42 for all six types of MD simulations and comparing time averaged quantities with those averaged over 10 replica trajectories. In line with the results for Aβ40 reported by Paul *et al.*,[70] we show that the N2CD of Aβ42 represents a better metric of convergence than the RMSD. Our results indicate that the N2CD is also more sensitive to trajectory-to-trajectory variability than the RMSD. In line with previous studies,[24,25,28] our results show that 10 replica MD trajectories of Aβ42 sample the conformational space more effectively than a single long MD trajectory, which is reflected in, for example, much higher occurrence of extreme values of N2CD distances (>6 nm and <2 nm) than reported by Paul and collaborators.[70]

Our simulations are based on CHARMM36m, which is one of the top MD force fields currently used in MD studies of IDPs. We assessed this force field with respect to experimental per-residue $^3J(H^N, H^{C\alpha})$ coupling constants for Aβ in aqueous solution reported by Roche and collaborators[71] and showed that while the MD-derived coupling constant reproduces the experimental data reasonably well, CHARMM36m underestimates experimental $^3J(H^N, H^{C\alpha})$ values within two hydrophobic regions, the MHR and CTR, of Aβ42, thereby underestimating the extended β-strand content in these two hydrophobic regions, in agreement with prior observations for Aβ40.[70] Notably, deviations of the MD-derived coupling constant values from the experimental counterparts are overall larger than the corresponding MD-derived salt-induced differences.

Not many previous MD studies addressed the effect of salt on Aβ conformational dynamics, although many of them used various levels of NaCl (50, 100, 150 mM) in their simulations to mimic physiological conditions.[20–22,70,75] Smith and Cruz studied the effect of various types of salt on conformational dynamics of Aβ(21–30) and reported that NaCl does not significantly affect the secondary structure of this decapeptide despite enhanced hydrogen bonding and increased turn stability.[76] Our results show that addition of 150 mM salt into water significantly decreases hydrophobic SASA of Aβ42 by increasing the compactness of the resulting conformational ensemble concomitant with formation of new long-range tertiary contacts and decreased coil content, in particular within the hydrophobic regions of Aβ42. Addition of lipids to Aβ42 in pure water exerts an opposite effect on the free energy landscapes by promoting more extended Aβ42 conformations. Interestingly, addition of both salt and lipids enhances the ruggedness of free energy landscapes of Aβ42 conformations.

MD simulations in CHARMM36m reported by Sciacca and collaborators examined 1 : 1 Aβ42/lipid complexes with two types of lipids, PC14 and PC22, to show that the hydrophobic effect drove protein–lipid interactions, which were further enhanced when Aβ42 monomer adopted α-helical conformations.[21] Fatafta *et al.* showed that Aβ42 formed stable complexes with one POPC or DPPC lipid as well as with three POPC lipids, whereby in the latter case Aβ42 exhibited a transition from predominantly coil to predominantly helical or β-sheet conformations.[22] In contrast to the above studies, we do not observe any significant helical content in Aβ42 in any of the six types of simulations. The per-residue helical propensities are the highest (up to 0.10) for Aβ42 interacting with 48 lipids in the absence of salt, whereas in the presence of salt these propensities are equal to zero. We find an increased propensity for Aβ42 to adopt turn structures when in a complex with 12 DMPC, which is consistent with Fatafta *et al.* who reported increased turn content for A*β*42 in a complex with one lipid molecule.[22] When Aβ42 is in a complex with 48 lipids, its β-strand propensities tend to increase, and a parallel β-sheet structure between the F4-D7 and I31-I32 regions emerges in the presence of salt. We show that lipids stabilize the turn in the CFR, which was posited to nucleate Aβ42 folding.[77] Overall, our results indicate that lipids decrease coil and increase turn and strand content, however, details of these secondary structure effects depend on the lipid concentration.

Using MD simulations, La Rosa and collaborators examined another IDP, 37 amino acids-long human islet amyloidogenic polypeptide (IAPP), in a complex with 1, 3, 6, and 10 DMPC lipids and concluded that IAPP–DMPC complex formation is driven by hydrophobic effect and that all complexes remained stable, whereby 6 DMPC lipids effectively saturated the IAPP binding site, forming hemicellar-like structures.[20] In line with these findings, our simulations also show that effective hydrophobic interactions stabilize Aβ42 in a complex with 12 or 48 DMPC lipids both in the absence and presence of salt. However, instead of saturation of a single binding site, our results showcase a great amount of structural flexibility in Aβ42, whereby addition of DMPC lipids facilitates partial unfolding and destabilizes tertiary contacts of the NTR with other Aβ42 regions. This structural flexibility is a fingerprint of IDPs, which are known to adapt their conformations depending on the binding partner.[78] Our calculation of the interface area between Aβ42 and the lipid cluster demonstrates that even in the presence of 48 lipid molecules, only about one third of the total SASA of Aβ42 is in contact with lipid molecules. Thus, Aβ42 remains adsorbed to the surface of a lipid cluster of 12 or 48 lipids, but does not penetrate it. We propose that the observed affinity of Aβ42 monomer to nucleate lipid self-assembly while remaining only partially adsorbed on the lipid cluster may play a role in mediating a physiological function of Aβ42, such as repairing leaks in the blood–brain barrier, whereby nucleating lipid assembly and delivering lipids to the leaky site without penetrating and thereby damaging the membrane would be critical.

Conflicts of interest

There are no conflicts to declare.

Acknowledgements

This work has been supported by the National Science Foundation through the grant numbers MCB-1817650 and OAC-1919691. MD simulations were performed on hardware supported by Drexel's University Research Computing Facility. The authors acknowledge fruitful discussions with Prof. Reinhard Schweitzer-Stenner on the comparison of MD-derived and experimental *J*-coupling constants.

Notes and references

1 C. L. Masters and D. J. Selkoe, *Cold Spring Harb. Perspect. Med.*, 2012, **2**, a006262.
2 G. Chen, T. Xu, Y. Yan, Y. Zhou, Y. Jiang, K. Melcher and H. E. Xu, *Acta Pharmacol. Sin.*, 2017, **38**, 1205–1235.
3 B. Urbanc, *Isr. J. Chem.*, 2017, **57**, 651–664.
4 F. Chiti and C. M. Dobson, *Annu. Rev. Biochem.*, 2006, **75**, 333–366.
5 T. L. Williams and L. C. Serpell, *FEBS J.*, 2011, **278**, 3905–3917.
6 S. A. Kotler, P. Walsh, J. R. Brender and A. Ramamoorthy, *Chem. Soc. Rev.*, 2014, **43**, 6692–6700.
7 E. S. Musiek and D. M. Holtzman, *Nat. Neurosci.*, 2015, **18**, 800–806.
8 J. T. Jarrett, E. P. Berger and P. T. Lansbury, *Ann. N. Y. Acad. Sci.*, 1993, **695**, 144–148.
9 J. T. Jarrett, E. P. Berger and P. T. Lansbury, *Biochemistry*, 1993, **32**, 4693–4697.
10 K. N. Dahlgren, A. M. Manelli, W. B. Stine, L. K. Baker, G. A. Krafft and M. J. LaDu, *J. Biol. Chem.*, 2002, **277**, 32046–32053.

11 P. Maiti, A. Lomakin, G. Benedek and G. Bitan, *J. Neurochem.*, 2010, **113**, 1252–1262.
12 K. Iijima, H. Liu, A. Chiang, S. Hearn, M. Konsolaki and Y. Zhong, *Proc. Natl. Acad. Sci. U. S. A.*, 2004, **101**, 6623–6628.
13 E. McGowan, F. Pickford, J. Kim, L. Onstead, J. Eriksen, C. Yu, L. Skipper, M. P. Murphy, J. Beard, P. Das, K. Jansen, M. Delucia, W.-L. Lin, G. Dolios, R. Wang, C. B. Eckman, D. W. Dickson, M. Hutton, J. Hardy and T. Golde, *Neuron*, 2005, **47**, 191–199.
14 H. M. Brothers, M. L. Gosztyla and S. R. Robinson, *Front. Aging Neurosci.*, 2018, **10**, 118.
15 S. J. Soscia, J. E. Kirby, K. J. Washicosky, S. M. Tucker, M. Ingelsson, B. Hyman, M. A. Burton, L. E. Goldstein, S. Duong, R. E. Tanzi and R. D. Moir, *PLoS One*, 2010, **5**, e9505.
16 D. K. Kumar, S. H. Choi, K. J. Washicosky, W. A. Eimer, S. Tucker, J. Ghofrani, A. Lefkowitz, G. McColl, L. E. Goldstein, R. E. Tanzi and R. D. Moir, *Sci. Transl. Med.*, 2016, **8**, 340ra72.
17 M. R. White, R. Kandel, S. Tripathi, D. Condon, L. Qi, J. Taubenberger and K. L. Hartshorn, *PLoS One*, 2014, **9**, e101364.
18 M. R. White, R. Kandel, I.-N. Hsieh, X. De Luna and K. L. Hartshorn, *PLoS One*, 2018, **13**, e0194001.
19 K. Bourgade, A. Le Page, C. Bocti, J. M. Witkowski, G. Dupuis, E. H. Frost and T. Fueloep, Jr., *J. Alzheimer's Dis.*, 2016, **50**, 1227–1241.
20 C. La Rosa, S. Scalisi, F. Lolicato, M. Pannuzzo and A. Raudino, *J. Chem. Phys.*, 2016, **144**, 184901.
21 M. F. Sciacca, F. Lolicato, C. Tempra, F. Scollo, B. R. Sahoo, M. D. Watson, S. Garcia-Vinuales, D. Milardi, A. Raudino, J. C. Lee, A. Ramamoorthy and C. La Rosa, *ACS Chem. Neurosci.*, 2020, **11**, 4336–4350.
22 H. Fatafta, B. Kav, B. F. Bundschuh, J. Loschwitz and B. Strodel, *Biophys. Chem.*, 2022, **280**, 106700.
23 R. D. Johnson, D. G. Steel and A. Gafni, *Protein Sci.*, 2014, **23**, 869–883.
24 L. S. D. Caves, J. D. Evanseck and M. Karplus, *Protein Sci.*, 1998, **7**, 649–666.
25 B. Knapp, L. Ospina and C. M. Deane, *J. Chem. Theory Comput.*, 2018, **14**, 6127–6138.
26 V. M. Burger, T. Gurry and C. M. Stultz, *Polymers*, 2014, **6**, 2684–2719.
27 J.-E. Shea and B. Urbanc, *Curr. Topics Med. Chem., Special Issue: Protein Misfolding in Conformational Disorders*, ed. C. M. Gomes, 2012, pp. 2596–2610, vol. 12.
28 B. Barz and B. Urbanc, *PLoS One*, 2012, **7**, e34345.
29 M. J. Voelker, B. Barz and B. Urbanc, *J. Chem. Theory Comput.*, 2017, **13**, 4567–4583.
30 J. Huang, S. Rauscher, G. Nawrocki, T. Ran, M. Feig, B. L. de Groot, H. Grubmüller and A. D. MacKerell, Jr., *Nat. Methods*, 2017, **14**, 71–73.
31 S. Zhang, R. Schweitzer-Stenner and B. Urbanc, *J. Chem. Theory Comput.*, 2020, **16**, 510–527.
32 S. Zhang, B. Andrews, R. Schweitzer-Stenner and B. Urbanc, *J. Phys. Chem. B*, 2020, **124**, 11600–11616.
33 B. Andrews, S. Zhang, R. Schweitzer-Stenner and B. Urbanc, *Biomolecules*, 2020, **10**, 1121.
34 B. Andrews, K. Long and B. Urbanc, *J. Phys. Chem. B*, 2021, **125**, 6897–6911.
35 B. Andrews, J. Guerra, R. Schweitzer-Stenner and B. Urbanc, *Phys. Chem. Chem. Phys.*, 2022, **24**, 3259–3279.
36 A. N. Siakotos, G. Rouser and S. Fleischer, *Lipids*, 1968, **4**, 234–239.
37 R. O. Calderon, B. Attema and G. H. DeVries, *J. Neurochem.*, 1995, **64**, 424–429.
38 H. J. C. Berendsen, D. van der Spoel and R. van Drunen, *Comput. Phys. Commun.*, 1995, **91**, 43–56.
39 E. Lindahl, B. Hess and D. van der Spoel, *J. Mol. Model.*, 2001, **7**, 306–317.
40 D. V. D. Spoel, E. Lindahl, B. Hess, G. Groenhof, A. E. Mark and H. J. C. Berendsen, *J. Comput. Chem.*, 2005, **26**, 1701–1718.
41 B. Hess, C. Kutzner, D. van der Spoel and E. Lindahl, *J. Chem. Theory Comput.*, 2008, **4**, 435–447.
42 S. Pronk, S. Pall, R. Schulz, P. Larsson, P. Bjelkmar, R. Apostolov, M. R. Shirts, J. C. Smith, P. M. Kasson, D. van der Spoel, B. Hess and E. Lindahl, *Bioinformatics*, 2013, **29**, 845–854.
43 S. Pall, M. J. Abraham, C. Kutzner, B. Hess and E. Lindahl, *Solving software challenges for exascale*, 2015, pp. 3–27.
44 M. J. Abraham, T. Murtola, R. Schulz, S. Páll, J. C. Smith, B. Hess and E. Lindahl, *SoftwareX*, 2015, **1–2**, 19–25.
45 A. D. MacKerell, D. Bashford, M. Bellott, R. L. Dunbrack, J. D. Evanseck, M. J. Field, S. Fischer, J. Gao, H. Guo, S. Ha, D. Joseph-McCarthy, L. Kuchnir, K. Kuczera, F. T. K. Lau, C. Mattos, S. Michnick, T. Ngo, D. T. Nguyen, B. Prodhom, W. E. Reiher, B. Roux, M. Schlenkrich, J. C. Smith, R. Stote, J. Straub, M. Watanabe, J. Wiorkiewicz-Kuczera, D. Yin and M. Karplus, *J. Phys. Chem. B*, 1998, **102**, 3586–3616.
46 A. D. MacKerell, M. Feig and C. L. Brooks, *J. Comput. Chem.*, 2004, **25**, 1400–1415.
47 R. B. Best, X. Zhu, J. Shim, P. E. M. Lopes, J. Mittal, M. Feig and A. D. MacKerell, Jr., *J. Chem. Theory Comput.*, 2012, **8**, 3257–3273.
48 R. W. Pastor and A. D. MacKerell, Jr., *J. Phys. Chem. Lett.*, 2011, **2**, 1526–1532.
49 B. Urbanc, J. M. Borreguero, L. Cruz and H. E. Stanley, *Methods Enzymol.*, 2006, **412**, 314–338.
50 B. Urbanc, L. Cruz, S. Yun, S. V. Buldyrev, G. Bitan, D. B. Teplow and H. E. Stanley, *Proc. Natl. Acad. Sci. U. S. A.*, 2004, **101**, 17345–17350.
51 S. Pall and B. Hess, *Comput. Phys. Commun.*, 2013, **184**, 2641–2650.
52 G. Bussi, D. Donadio and M. Parrinello, *J. Chem. Phys.*, 2007, **126**, 014101.
53 H. J. C. Berendsen, J. P. M. Postma, W. F. van Gunsteren, A. DiNola and J. R. Haak, *J. Chem. Phys.*, 1984, **8**, 3684–3690.
54 S. E. Feller, Y. H. Zhang, R. W. Pastor and B. R. Brooks, *J. Chem. Phys.*, 1995, **103**, 4613–4621.
55 Q. Ke, X. Gong, S. Liao, C. Duan and L. Li, *J. Mol. Liq.*, 2022, **365**, 120116.
56 M. Karplus, *J. Chem. Phys.*, 1959, **30**, 11–15.

57 J.-S. Hu and A. Bax, *J. Am. Chem. Soc.*, 1997, **119**, 6360–6368.
58 G. W. Vuister and A. Bax, *J. Am. Chem. Soc.*, 1993, **115**, 7772–7777.
59 M. Habeck, W. Rieping and M. Nilges, *J. Magn. Reson.*, 2005, **177**, 160–165.
60 B. Vögeli, J. Ying, A. Grishaev and A. Bax, *J. Am. Chem. Soc.*, 2007, **129**, 9377–9385.
61 K. W. Plaxco, K. T. Simons and D. Baker, *J. Mol. Biol.*, 1998, **277**, 985–994.
62 M. Heinig and D. Frishman, *Nucleic Acids Res.*, 2004, **32**, W500–W502.
63 W. Humphrey, A. Dalke and K. Schulten, *J. Mol. Graphics*, 1996, **14**, 33–38.
64 R. T. McGibbon, K. A. Beauchamp, M. P. Harrigan, C. Klein, J. M. Swails, C. X. Hernandez, C. R. Schwantes, L.-P. Wang, T. J. Lane and V. S. Pande, *Biophys. J.*, 2015, **109**, 1528–1532.
65 G. Kaminski, E. M. Duffy, T. Matsui and W. L. Jorgensen, *J. Phys. Chem.*, 1994, **98**, 13077–13082.
66 G. A. Kaminski, R. A. Friesner, J. Tirado-Rives and W. L. Jorgensen, *J. Phys. Chem. B*, 2001, **105**, 6474–6487.
67 B. Milorey, R. Schweitzer-Stenner, B. Andrews, H. Schwalbe and B. Urbanc, *Biophys. J.*, 2021, **120**, 662–676.
68 T. L. Williams, B. J. Johnson, B. Urbanc, A. T. A. Jenkins, S. D. Connell and L. C. Serpell, *Biochem. J.*, 2011, **439**, 67–77.
69 T. L. Williams, L. C. Serpell and B. Urbanc, *Biochim. Biophys. Acta, Proteins Proteomics*, 2016, **1864**, 249–259.
70 A. Paul, S. Samantray, M. Anteghini, M. Khaled and B. Strodel, *Chem. Sci.*, 2021, **12**, 6652–6669.
71 J. Roche, Y. Shen, J. H. Lee, J. Ying and A. Bax, *Biochemistry*, 2016, **55**, 762–775.
72 M. Karplus, *J. Am. Chem. Soc.*, 1963, **85**, 2870–2871.
73 N. Xiang, Y. Lyu, X. Zhu and G. Narsimhan, *Phys. Chem. Chem. Phys.*, 2018, **20**, 6817–6829.
74 A. Quist, I. Doudevski, H. Lin, R. Azimova, D. Ng, B. Frangione, B. Kagan, J. Ghiso and R. Lal, *Proc. Natl. Acad. Sci. U. S. A.*, 2005, **102**, 10427–10432.
75 H. Fatafta, M. Khaled, M. C. Owen, A. Sayyed-Ahmad and B. Strodel, *Proc. Natl. Acad. Sci. U. S. A.*, 2021, **118**, e2106210118.
76 M. D. Smith and L. Cruz, *J. Phys. Chem. B*, 2013, **117**, 6614–6624.
77 N. D. Lazo, M. A. Grant, M. C. Condron, A. C. Rigby and D. B. Teplow, *Protein Sci.*, 2005, **14**, 1581–1596.
78 B. Strodel, *J. Mol. Biol.*, 2021, **433**, 167182.